Universitat Politècnica de Catalunya
Programa de Doctorat de Matemàtica Aplicada

Engineering patterns of wrinkles and bubbles in supported graphene through modeling and simulation

by Kuan Zhang

Doctoral Thesis

Advisor: Marino Arroyo

Barcelona, March 2015

Abstract

Engineering patterns of wrinkles and bubbles in supported graphene through modeling and simulation

Kuan Zhang

Graphene deposited on a substrate often exhibits out-of-plane deformations with different features and origins. Networks of localized wrinkles have been observed in graphene synthesized through CVD, as a result of compressive stresses transmitted by the substrate. Graphene blisters have been reported with various sizes and shapes, and have been shown to be caused by gas trapped between graphene and substrate. Such wrinkles or bubbles locally modify the electronic properties and are often seen as defects. It has been also suggested that the strong coupling between localized deformation and electronic structure can be potentially harnessed in technology by strain engineering, although it has not been possible to precisely control the geometry of out-of-plane deformations, partly due to an insufficent theoretical understanding of the underlying mechanism, particularly under biaxial strains.

The specific contributions of the thesis are outlined next. Firstly, we study the emergence of spontaneous wrinkling in supported and laterally strained graphene with high-fidelity simulations based on an atomistically informed continuum model. With a simpler theoretical model, we characterize the onset of buckling and the nonlinear behavior after the instability in terms of the adhesion and frictional material parameters of the graphene-substrate interface. We find that a distributed rippling linear instability transits to localized wrinkles due to the nonlinearity in the van der Waals graphene-substrate interactions. We identify friction as a selection mechanism for the separation between wrinkles, because the formation of far apart wrinkles is penalized by the work of friction.

Secondly, we examine the mechanics of wrinkling in supported graphene upon biaxial strains. With realistic simulations and an energetic analysis, we understand how strain anisotropy, adhesion and friction govern spontaneous wrinkling. We then propose a strategy to control the location of wrinkles through patterns of weaker adhesion. These mechanically self-assembled networks are stable under the pressure produced by an enclosed fluid and form continuous channels, opening the door to nano-fluidic applications.

Finally, we examine the coexistence of wrinkles and blisters in supported graphene. By

changing the applied strain and gas mass trapped beneath the graphene sample, we build a morphological diagram determining the size and shape of graphene bubbles, and their coexistence with wrinkles. As a whole, the research described above depicts a systematic and broad understanding of out-of-plane deformations in monolayer graphene on a substrate, and could be a theoretical foundation towards strain engineering in supported graphene.

Acknowledgments

I would like to offer my sincerest gratitude to my advisor, Professor Marino Arroyo, for opening me the doors of a very exciting research topic, teaching me with his patience and knowledge, and encouraging me with a lot of freedom to explore it. It has been an honor and a privilege to work with him and I am deeply grateful for the opportunity to have done so.

I am greatly thankful to the faculty of LaCàN and Departament de Matemàtica Aplicada III, in particular, Professors Antonio Huerta, Pedro Díez, Antonio Rodríguez and Irene Arias. Without their support, this project would not have been possible. I would also like to thank the reviewers of the thesis and the members of the committee for their useful comments and advice.

It has been a privilege to share so many moments with my officemates and fellow post-graduate students in the group of LaCàN. Among them I want to mention specially Adrian, Daniel, Amir, Mohammad, Christian, Behrooz, David, Alejandro, Dimitri, Aditya, and Bin. I am very grateful for their true friendship and support through the years.

I owe sincere and earnest thankfulness to my family, especially my mother, with their always and unconditional support and encouragement. Their love has provided me with the enthusiasm to face new projects and constantly seek novel challenges. I just want to thank them for that.

Finally, my thanks also go to those who, directly or indirectly, helped me to finish my thesis.

I want to thank the support of UPC-FPI Grant, and the European Research Council (240487).

Contents

List of Figures

Thesis body

Chapter 1

Introduction

Graphene is a single layer of carbon atoms densely packed in a two-dimensional hexagonal lattice. As an abundant element in the universe, carbon is incredibly versatile as the chemical basis for all known life on earth. Depending on the arrangement of atoms, it can form hard diamond or soft graphite. Graphene is another allotrope of carbon with 2-dimensional properties. In graphene, atoms adopt a planar structure with sp2 bonds of length 0.142 nm. It is the thinnest and lightest material ever known. Since the discovery of graphene in 2004 (Novoselov et al., 2004), it has attracted considerable attention due to its exceptional structure, mechanical, chemical and electronic properties, which offer unique possibilities in nanostructured materials and devices (Meyer et al., 2007; Bunch et al., 2007; Lee et al., 2009). Graphene is an excellent conductor of electricity, because electrons can move through graphene extremly fast. It is also the best heat conductor.

Many unique mechanical properties of graphene result from its 2D lattice structure. Interestingly, it was theoretically predicted in 1940s that a two dimensional material could not exist, because it would be unstable in front of thermal fluctuation (Landau and Lifshitz, 1980; Peierls, 1935). The debate between the theory that strict 2D membrane would be thermodynamically unstable and the experimental observations could be clarified by the coupling between bending and stretching in the out-of-plane fluctuations, when described with a geometrically nonlinear theory (Meyer et al., 2007; Nelson and Peliti, 1987).

Graphene is easily bendable but very hard to stretch. Free-standing graphene is prone to relaxing in-plane deformations by spontaneous ripples, see Fig. 1.1(a). Regular ripples can be also formed under different conditions, such as in-plane shear (Duan et al., 2011)

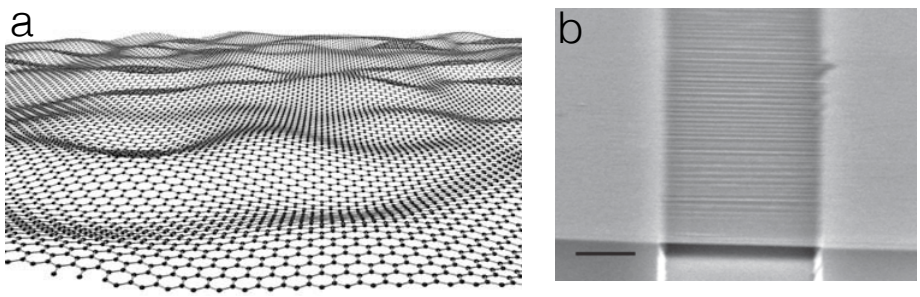

Figure 1.1: (a): a perspective view on random rippling in free-standing graphene (Meyer et al., 2007). (b): regular ripples in suspended graphene (Bao et al., 2009).

or indentation (Huang and Zhang, 2011; Ghosh and Arroyo, 2013). Several attempts have focused on controlling ripple structure in suspended graphene, with potential applications in graphene electronics through strain (Bao et al., 2009), see Fig. 1.1(b).

As a result of the synthesis process or performing as a functional material, graphene is often supported on a substrate. Rather than a flatland, supported graphene describes a landscape shaped by out-of-plane features with different physical origins. Defects such as dislocations or grain boundaries can relax through out-of-plane deformations (Liu and Yakobson, 2010; Yakobson and Ding, 2011; Zhang et al., 2014), which have been observed experimentally (Duong et al., 2012; Warner et al., 2013). Localized wrinkles are commonly observed in single or few-layer graphene grown by chemical vapor deposition (CVD) on solid metallic substrates (Li et al., 2009; Kim et al., 2011; Robertson et al., 2011). Such wrinkles are formed by the lateral strain produced upon cooling of graphene due to the differential thermal expansion between graphene and the substrate (Obraztsov et al., 2007). This process usually forms networks with a typical spacing between hundreds of nanometers and a few microns, see Fig. 1.2(a-b). Beyond isolated wrinkles, massive crumpling and delamination has been reported in supported multilayer graphene under very large biaxial compression (Zang et al., 2013). Gas trapped between graphene and the substrate, either unintentionally (Stolyarova et al., 2009; Georgiou et al., 2011) or in a controlled manner (Bunch et al., 2008; Koenig et al., 2011; Zabel et al., 2012; Pan et al., 2012; Kitt et al., 2013), can elastically deform graphene, producing blisters of various shapes and sizes, see Fig. 1.2(c-d). Indeed, it has been shown that graphene is highly impermeable to common gases. The large elastic strain caused by these out-of-plane deformations disrupts the electronic structure of pristine graphene (Xu et al., 2009; Levy et al., 2010; Zabel et al., 2012). For this

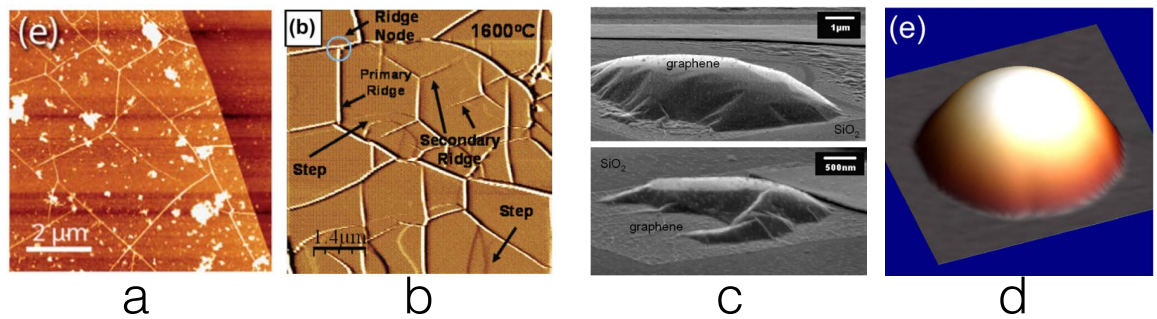

Figure 1.2: (a-b): wrinkling networks in supported graphene (Calado et al., 2012; Prakash et al., 2010). (c-d): observations about graphene blisters in experiment (Stolyarova et al., 2009; Georgiou et al., 2011).

reason, wrinkles and blisters are generally perceived as defects in graphene-based electronics (Zhu et al., 2012; Jiang et al., 2013) and optics (Garcia-Pomar et al., 2013).

It has been also suggested, however, that the strong coupling between localized deformation and electronic structure can be potentially harnessed by strain engineering (Levy et al., 2010; Castellanos-Gomez et al., 2013; Ruoff, 2012; Pereira et al., 2010; Zabel et al., 2012). A number of experimental strategies have attempted to control wrinkle networks in graphene. It has been shown that the transfer process can increase, decrease, or even eliminate wrinkling (Liu et al., 2011; Calado et al., 2012), and that wrinkles preferentially form at topographical features of the substrate (Kim et al., 2011; Pan et al., 2011; Liu et al., 2012). However, it has not been possible to precisely control their geometry, partly due to an insufficient theoretical understanding.

In fact, there has been intense research in the formation of buckling patterns in the laterally compressed systems consisting of an elastic film coupled to a substrate. It has been shown that the generic linear instability consisting of sinusoidal ripples evolves upon further compression either by coarsening (Brau et al., 2011; Cao et al., 2012) or by forming localized wrinkles (Leahy et al., 2010; Holmes and Crosby, 2003). For example, uniaxially compressed elastic films floating on a fluid develop curvature localization after a uniformly periodic rippling with a characteristic wavelength (Pocivavsek et al., 2008; Audoly, 2011), see Fig. 1.3(a). In this system, the ripple-to-wrinkle transition occurs when the film is compressed beyond a third of its initial ripple wavelength, and has been attributed to geometric nonlinearity. In a different context, a ripple-to-wrinkle transition has been explained by the

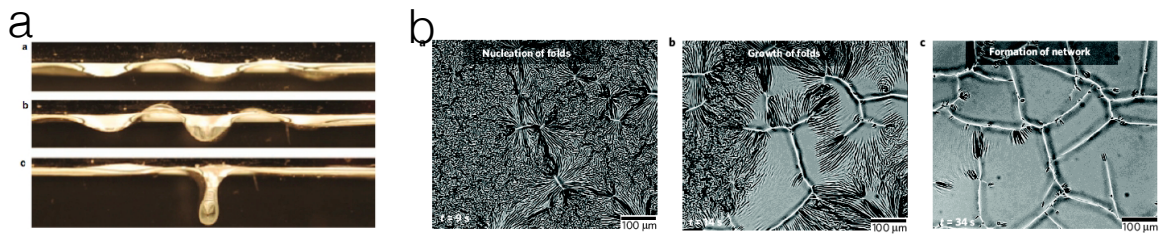

Figure 1.3: (a): a ripple-to-wrinkle transition in supported thin film upon uniaxial compression (Pocivavsek et al., 2008). (b): formation of wrinkle network upon biaxial compression (Kim et al., 2011).

nonlinearity of a deformable substrate (Zang et al., 2012). Under biaxial compression, the process of formation of wrinkle network has been reported (Kim et al., 2011), see Fig. 1.3(b).

The goal of this thesis is to understand the mechanics underlying the emergence of out-of-plane deformations in supported graphene upon compressive strain and interstitial pressure, and to propose strategies to precisely control the patterns of wrinkles and blisters.

The thesis is organized around the following questions about the mechanics of monolayer graphene supported on a substrate.

1. **Spontaneous wrinkling upon compressive strains.** Generically, localized wrinkling develops from distributed ripping as a result of nonlinearity in the system. A first question is if this is also the case for supported graphene interacting with a substrate through weak van der Waals forces. If this is the case, what is the source of nonlinearity that drives the localization of deformation? What is the key factor determining the separation between wrinkles? What determines the morphology of wrinkle networks, presumably developing under biaxial compression? What is the effect of the graphene-substrate interactions and of strain anisotropy on the wrinkle network?

2. **Control of strain-engineered wrinkle networks.** Based on the understanding gained about spontaneous wrinkling, is it possible to propose a strategy to control the location of wrinkles? Since wrinkles could be potentially used as channels in nano-fluidic applications, are the wrinkle networks stable under the pressure produced by an enclosed fluid?

3. **Graphene blisters and wrinkles.** Can we provide a unified mechanical picture of out-of-plane features in supported graphene, describing the formation of wrinkles, blisters,

and their coexistence?

To address these questions, we will resort to high-fidelity continuum simulations. The modelling methodology is presented in Chapt. 2. The first contribution mentioned above is split into two chapters. Chapt. 3 presents the simulation result and a theory to analyze the uniaxial wrinkling of supported graphene, while Chapt. 4 examines the wrinkling upon biaxial compressive strains. The second contribution is in Chapt. 5. Chapt. 6 describes the last one. In each of chapters the most significant contributions are highlighted. Research ideas emerging from the work performed are proposed after a conclusion in Chapt. 7.

Chapter 2

Computational modelling of supported graphene

Molecular dynamics (MD) and molecular mechanics (MM) are mature techniques to simulate the mechanics of nanostructure, e.g. graphene and carbon nanotubes (Bernholc et al., 1998; Gao et al., 1998). However, a graphene sample of 1 μm^2 includes approximately 3.8×10^7 atoms, which makes all-atom computations unpractical. The pioneering work of Yakobson about 20 years ago adopted the theory of elastic shells to study the buckling patterns of compressed carbon nanotubes, and showed that continuum mechanics could be applied to carbon nanostructures down to nanometer scales (Yakobson et al., 1996). In parallel, significant research was devoted to connecting atomistic models of materials and continuum mechanics, notably with the quasicontinuum methods (Shenoy et al., 1998; Tadmor et al., 1999; Smith et al., 2000). Away from defects and for stable crystals, it was shown that the Cauchy-Born rule could be used to connect atomistic and continuum deformation, thereby allowing researchers to define hyper-elastic potentials directly from the atomistic potentials. However, for curved crystalline films such as graphene, the CB rule was shown to be inconsistent, and was generalized by an exponential Cauchy-Born rule in Arroyo and Belytschko (2002). It has been demonstrated that such continuum models can accurately describe the mechanics of graphene and carbon nanotubes in the full nonlinear regime in the absence of defects (Arroyo and Belytschko, 2004a, 2003; Zhang et al., 2005; Wu et al., 2008; Arias and Arroyo, 2008). Other types of atomistic-based continuum methods have also been proposed, e.g. higher-order Cauchy-Born rule (Guo et al., 2006), to take into

account of the curvature of the graphene surface.

Here, we use this model for the elastic behavior of graphene. However, to model supported graphene, the interaction with the substrate is equally important, and is developed in subsequent sections.

1 Model setup

The target of our modeling is to investigate the out-of-plane deformations in supported graphene, see Fig. 2.1(a) for a clear definition of *ripples* and *wrinkles*. Fig. 2.1(b) depicts the model setup, in which a mesoscopic (of about 500×500 nm^2) graphene sample is adhered on a substrate undergoing lateral deformation. The domain is large enough to capture the typical wrinkle separation (several 100 nm) but small enough to be computationally tractable, since the geometric features of an individual wrinkle ($\sim$ 1 nm) (Zhu et al., 2012; Liu et al., 2012) need to be resolved. Graphene interacts with the substrate non-covalently, resulting in perpendicular adhesive forces and tangential frictional forces opposing sliding, see Fig. 2.1(c).

We use periodic boundary conditions and apply strain by progressively reducing the lateral dimensions of the periodic simulation box. The strain is viewed as externally applied by deforming the substrate, although it can occur from differential thermal expansion, as in graphene synthesis by CVD. We denote by λ_x and λ_y the stretch ratios between the current and initial lateral dimension along each coordinate, and by $\varepsilon_c = 1 - \lambda_x \lambda_y$ the compressive areal strain (normalized area difference). Here, we assume that the strain in the graphene sample is equal to the strain applied to the substrate and transmitted by the shear stress in the interface. In general, the deformation of the graphene sample and that of the substrate in its vicinity will not uniformly conform to the externally applied strain. Near to the edges of graphene, only a fraction of the applied strain is transmitted by the laterally deformed substrate. A shear lag model has been proposed in literature to explain this effect, see Fig. 2.2. It was found that a length in the order of 1-2 μm of graphene sample is needed for an efficient transfer of the applied strain from the substrate to graphene (Gong et al., 2010). In our case, a periodic simulation box represents a portion of a large graphene sample, where efficient strain transfer occurs. Furthermore, we assume that the substrate remains planar, which is generally the case although very soft substrates have been shown to ripple along

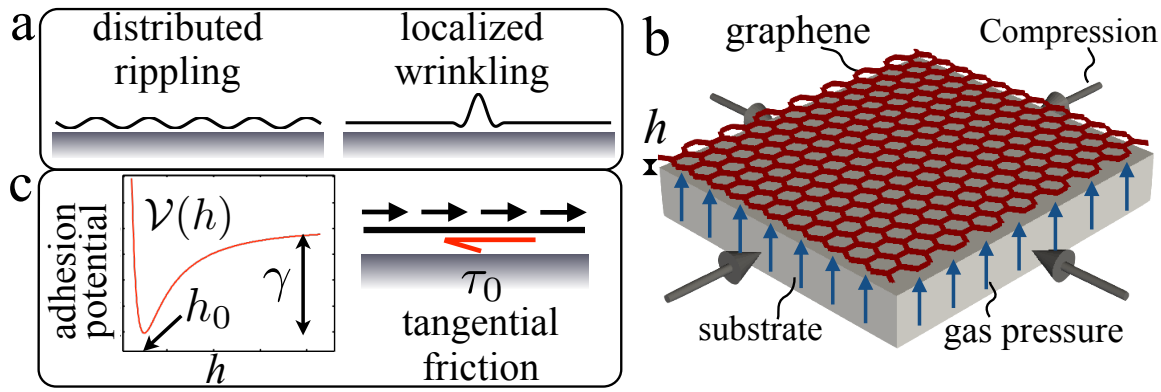

Figure 2.1: (a) Upon compression, confined thin films develop a variety of out-of-plane deformations, classified here as *rippling*, distributed wave-like disturbances, or *wrinkling*, localized out-of-plane features surrounded by planar regions. (b) Model setup for a graphene flake adhered to a substrate, laterally compressed and upon pressure by an enclosed fluid in the interface. h is the graphene-substrate separation. (c) Graphene interacts with the substrate through an adhesion potential $\mathcal{V}(h)$ (Aitken and Huang, 2010), characterized by the adhesion energy γ and the equilibrium separation h_0, and through tangential forces opposing sliding, modeled as dry friction with interfacial shear strength τ_0 (Zhang and Arroyo, 2013).

with graphene (Wang et al., 2011).

In the simulations, we apply strain incrementally by setting the stretch ratios at load increment k to $\lambda_{x,k} = (\delta\lambda_x)^k$ and $\lambda_{y,k} = (\delta\lambda_y)^k$, where $\delta\lambda_x$ denotes the incremental stretch ratio along x. To obtain the equilibrium configuration at step $k+1$, we modify the previous equilibrium configuration $\boldsymbol{x}_k(u,v)$ following $(\delta\lambda_x x_k(u,v), \delta\lambda_y y_k(u,v), z_k(u,v))$ to define an initial guess in the iterative procedure consistent with the boundary conditions.

2 Model for elasticity of graphene

We model graphene with an atomistic-based continuum method, which is geometrically exact. The internal energy per unit underformed surface is given by a hyper-elastic potential $W(\boldsymbol{C}, \mathfrak{K})$ that depends on the in-plane strain (the metric tensor) of the surface $\boldsymbol{C}$ measured through the right Cauchy-Green deformation tensor, and its curvature (the second fundamental form) $\mathfrak{K}$ (Arroyo and Belytschko, 2002). The potential W is systematically derived from the Brenner atomistic interactions describing the bonded energy and forces (Brenner,

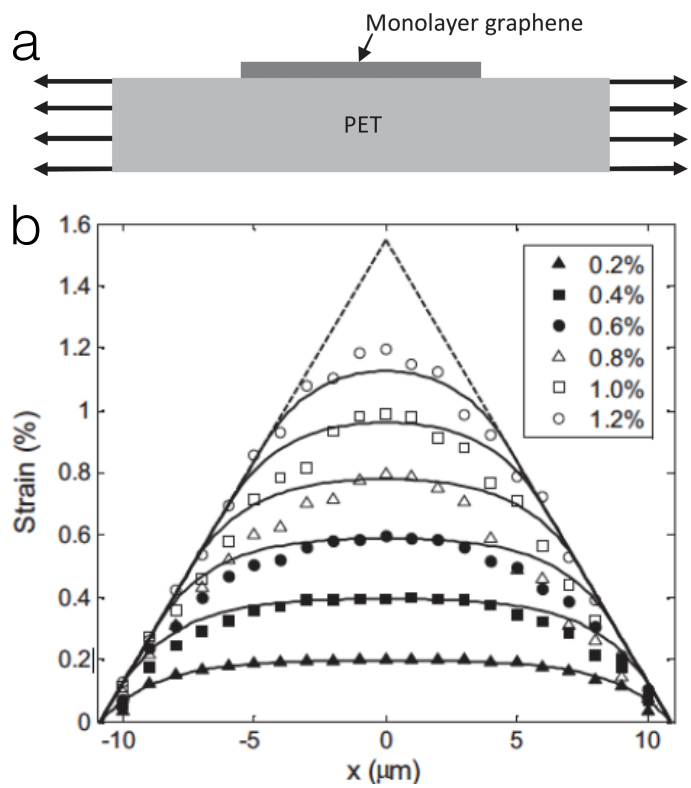

Figure 2.2: (a) Experimental setup, in which a sample of monolayer graphene is supported on a substrate upon uni-axial stretch. It has been shown experimentally that lateral strain is transmitted from the substrate to graphene flakes by frictional forces (Jiang et al., 2013). These frictional forces can in principle laterally deform a compliant substrate non-uniformly, so that the local strain of the substrate near the interface deviates from the applied strain. (b) shows strain distributions in graphene, comparing experimental results from the Raman measurements (symbols) with a nonlinear shear lag analysis (lines). For moderate strains and in the centre of the sample, the strain in the graphene flake conforms to the strain applied to the substrate. However, as stretch increases, the flake laterally slides near its edges, where the strain distribution becomes linear.

1990) using a kinematic rule linking continuum and lattice deformations, the exponential Cauchy-Born rule, and averaging the atomistic energy in one unit cell of the lattice. This model has been shown to very accurately mimic all-atom simulations with finite deformations and buckling instabilities (Arroyo and Belytschko, 2004b). The total elastic energy of the graphene sheet is then

$$U_{el}[\boldsymbol{x}] = \int_{\Omega_0} W(\boldsymbol{C}, \boldsymbol{\mathcal{K}})\ dS_0, \tag{2.1}$$

where S_0 is a reference stress-free planar state.

When this model is linearized around the planar ground state of graphene, the in-plane and bending elasticities are isotropic, and can be characterized by a surface Young's modulus Y_s (with units of line tension), a Poisson ratio ν, and a bending modulus D (Arroyo and Belytschko, 2004a; Lu et al., 2009). For the model used here, we have $Y_s = 336$ N m^{-1}, $\nu = 0.165$, $D = 0.238$ nN nm, consistent with experimental and *ab initio* calculations (Arroyo and Belytschko, 2004a; Lu et al., 2009; Lee et al., 2008).

3 Model for the graphene-substrate adhesive interaction

To model the non-bonded interaction between graphene and the substrate, we adopt a simple and generic Lennard-Jones potential(Girifalco et al., 2000). The pair-wise Lennard-Jones 6-12 potential between a graphene and a substrate atom a distance r apart is

$$V(r) = 4\epsilon \left[-\left(\frac{\sigma}{r}\right)^6 + \left(\frac{\sigma}{r}\right)^{12} \right], \tag{2.2}$$

where $r_0 = \sqrt[6]{2}\sigma$ is the equilibrium distance at which the potential attains its minimum, and ϵ is the energy at the equilibrium distance. These atom-atom interactions result in an effective point-half space interaction energy (per unit undeformed surface area) of the form (Aitken and Huang, 2010)

$$\mathcal{V}(h) = -\gamma \left[\frac{3}{2} \left(\frac{h_0}{h}\right)^3 - \frac{1}{2} \left(\frac{h_0}{h}\right)^9 \right], \tag{2.3}$$

where h is the separation between a given point and the planar substrate, h_0 is the equilibrium separation between the elastic sheet and a half-space, and γ denotes the well depth or adhesion energy.

We often adopt $\gamma = 0.45$ J/m^2, typical of the interaction between graphene and SiO_2 (Koenig et al., 2011), half of than that reported for copper (Yoon et al., 2012), but a few times larger than that on polydimethylsiloxane (Scharfenberg et al., 2012). As for the equilibrium separation h_0, which controls the decohesion separation and also the stiffness of this interaction, we range from 0.5 nm, in the order of that measured on SiO_2 (Gupta et al., 2006) to 6 nm, comparable to that reported for a polymeric substrate (Wang et al., 2011; Aitken and Huang, 2010; Gao and Huang, 2011). A larger equilibrium separations could be interpreted as an effective property for substrates that are not atomically flat. Substrate roughness has been shown to modify the effective adhesion energy and equilibrium separation when the wavelength of roughness is comparable to the equilibrium separation (Aitken and Huang, 2010; Gao and Huang, 2011). More discussions about the choice of material parameters and their impact on the behaviour of the system can be found at Zhang and Arroyo (2013).

4 Model for the friction between graphene and substrate

We model the tangential forces between graphene and substrate as dry friction (Zhang and Arroyo, 2013, 2014). Since dry friction results in a non-smooth model, we consider a regularized model of friction for numerical convenience with an incremental work of friction of the form

$$U_{fr,k}[\boldsymbol{x}] = \int_{\Omega_0} \tau_0 K(s_k(u,v))\, dS_0, \tag{2.4}$$

where τ_0 is the interfacial shear strength, s_k is the incremental lateral sliding relative to the substrate

$$s_k^2(u,v) = [x - \delta\lambda_x x_k(u,v)]^2 + [y - \delta\lambda_y y_k(u,v)]^2\,, \tag{2.5}$$

and $K(t)$ is a differentiable approximation to $|t|$. Here, we consider the log-sum-exp regularization

$$K(t) = \frac{1}{\beta}\log\left(e^{\beta t} + e^{-\beta t}\right) \tag{2.6}$$

for $\beta > 0$. As $\beta \to +\infty$, it can be shown that this family of smooth functions converges to the absolute value function. In our calculations, we choose $\beta = 200$ nm^{-1}. The quantity $1/\beta = 1/200$ nm can be interpreted as the length-scale over which the cusp of the absolute value around zero is being rounded, and therefore for sliding displacements larger than $1/\beta$,

$K(t)$ is indistinguishable from $|t|$ and we recover dry friction. We have checked that the results are insensitive to selecting larger values for β, which make numerical convergence more difficult.

For the interfacial shear strength upon sliding τ_0, we range from 0.3 to 4 MPa, comparable to measurements of graphene on polyethylene terephthalate (Jiang et al., 2013) and on silicon (Kitt et al., 2013).

5 Model for gas trapped in the interstitial space

Following the ideal gas law, we model the effect of gas molecules trapped in the interstitial space between graphene and the substrate by appending the free energy with the term

$$U_{pre} = -nRT \ln(V/V_0), \tag{2.7}$$

where n is the number of moles of gas trapped underneath the membrane, R is the ideal gas constant, T the absolute temperature, and V_0 an arbitrary reference volume. In simulations, we increase n incrementally, and obtain the pressure $p = nRT/V$ and the volume as part of the analysis. This protocol allows us to follow processes in a stable manner in which the pressure is not monotonic, and is also relevant to some experimental setups (Boddeti et al., 2013). For an enclosed fluid, invoking molecular incompressibility instead of the ideal gas law, this ensemble results in prescribing the enclosed volume.

To take into account of Equation (2.7), the enclosed volume and its variation need to be computed. The calculation of the volume can be recast into a surface integral by noting that $div\ \boldsymbol{x} = 3$ and invoking the divergence theorem

$$V = \frac{1}{3}\int_\Omega \text{div}\ \boldsymbol{x}\ dV = \frac{1}{3}\int_\Gamma \boldsymbol{x}\cdot\boldsymbol{n}\ dS, \tag{2.8}$$

where $\boldsymbol{n}$ is the outward normal to Γ.

An infinite volume is enclosed between the surface extended by periodicity (graphene) and a horizontal plane (the substrate), but a finite volume of each repeated cell can be defined. In this case, Equation (2.8) cannot be directly applied as the periodic surface has fictitious boundaries. A detailed treatment of this issue can be found in Rahimi et al. (2015), where we show that a proper formulation includes, in addition to the surface contribution in Equation (2.8), two line and a point contributions. Not including these extra terms results

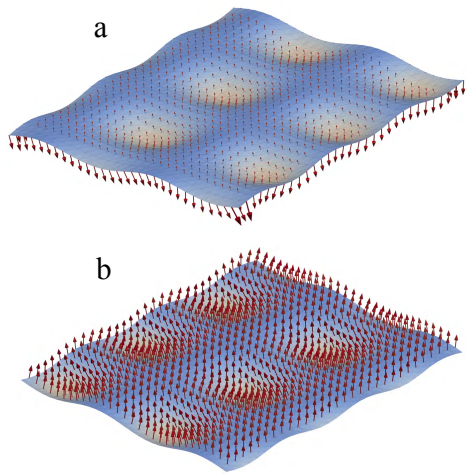

Figure 2.3: Nodal forces resulting from a follower pressure on a doubly periodic surface discretized with subdivision finite elements. The color map represents the deviation from a planar surface. In (a), unphysical forces appear near the boundaries of the computational domain if the line and point contributions to the volume and its variation are omitted. In contrast, (b) shows the correct distribution of nodal forces on the sheet.

in incorrect pressure forces as illustrated in Fig. 2.3.

6 Complete model and solution method

Denoting by $\boldsymbol{x}$ a parametrization of the graphene sheet and orienting x_3 perpendicular to the substrate, the total work function can be written as

$$U[\boldsymbol{x}] = \int_{\Omega_0} W(\boldsymbol{C}, \boldsymbol{\mathcal{K}})\ dS_0 + \int_{\Omega_0} \mathcal{V}(x_3)\ dS_0 + U_{fr,k}[\boldsymbol{x}] + U_{pre}, \tag{2.9}$$

where Ω_0 is the reference domain of the graphene membrane.

Equation (2.9) is discretized with subdivision finite elements (Cirak et al., 2000), which provide a smooth parametrization with square integrable curvature. At each strain increment, we obtain stable equilibrium configurations by numerical minimization using a quasi-Newton method combined with line-search (Arroyo and Belytschko, 2004b).

We present here two examples to verify our modeling. Firstly, we simulate a periodic graphene sample on a substrate and subject it to interstitial pressure but no strain. For a moderate number of trapped molecules, we expect that the solution will be a planar graphene sheet, displaced a small distance away from the equilibrium separation of the Lennard-Jones

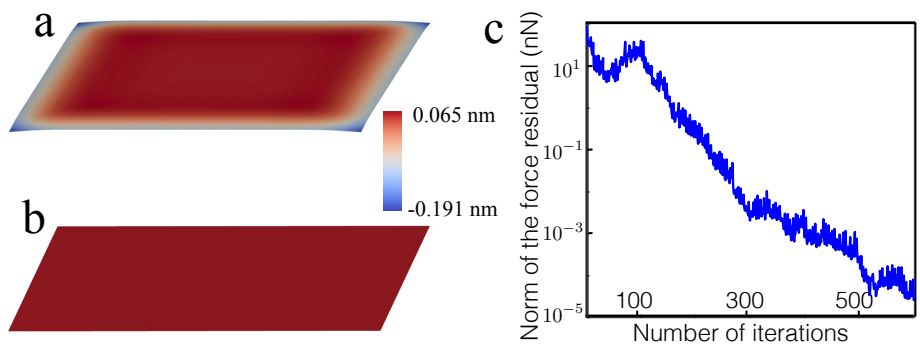

Figure 2.4: Nodal forces resulting from a follower pressure on a doubly periodic surface discretized with subdivision finite elements. The color map represents the deviation from a planar surface. In (a), unphysical forces appear near the boundaries of the computational domain. In contrast, (b) shows the correct distribution of nodal forces on the sheet.

adhesion potential, h_0. Fig. 2.4(a) shows that, when the boundary and corner terms of the volume and its variation are ignored (see Sec. 5), the result after the quasi-Newton iteration exhibits spurious deformations at the boundary of the periodic domain. In contrast, the correct calculation of the volume and its variation results in a planar state as expected, see Fig. 2.4(b). The numerical convergence of the iterative method is shown in Fig. 2.4(c). Secondly, we simulate the shear lag effect of friction between graphene and substrate (see a discussion about shear lag effect in Sec. 1). As expected, our model predicts a similar strain distribution on graphene as recorded from experiments (Fig. 2.2).

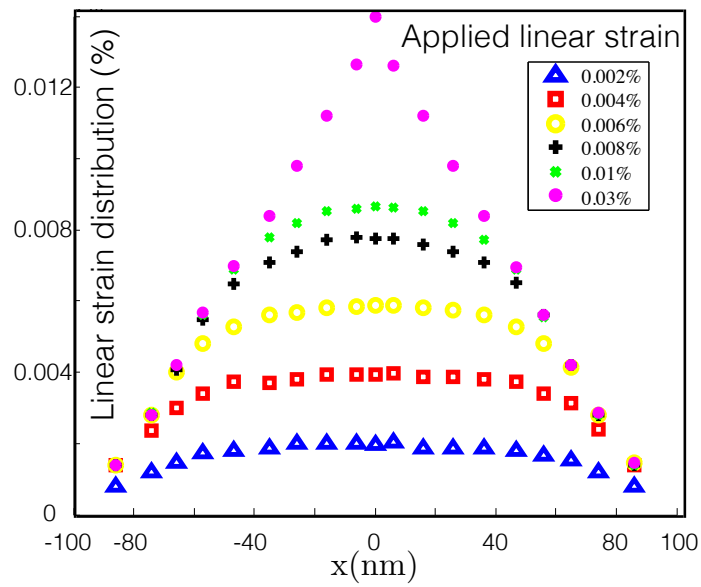

Figure 2.5: The predicted strain distribution of graphene from our simulation conforms with the experimental data from Fig. 2.2 and Jiang et al. (2013).

Chapter 3

Spontaneous wrinkling upon uniaxial compression

When deposited on a super soft substrate and compressed uniaxially, graphene has been shown to deform together with the substrate surface to develop distributed rippling (Wang et al., 2011). Here we focus on stiffer substrates, whose surface is assumed to remain planar. Consequently, any out-of-plane deformation of graphene such as wrinkling involves delamination. Figure 3.1 shows a typical numerical simulation exhibiting rippling and wrinkling. A periodic graphene slab with length $L_0 = 200$ nm is uniaxially compressed by incrementally decreasing the periodic length along one coordinate by a factor, $L_n = f^n L_0$ with $0 < f < 1$, where in practice f is close to one. For simplicity, in this simulation we ignore the effect of friction and pressure, which will be considered and discussed later. Initially, the graphene slab stays planar until, beyond a threshold, it develops periodic, small amplitude ripples, Fig. 3.1(b). As in similar systems (Pocivavsek et al., 2008; Im and Huang, 2008), the finite wavelength is set by a competition between bending energy, which penalizes high frequency undulations, and the interaction with the substrate, which penalizes large amplitude and low frequency out-of-plane deviations. By further compressing the sample, the out-of-plane deformation localizes into a single, sharp wrinkle, Fig. 3.1(c). The details of this generic process, e.g. the critical strain or the rippling and wrinkling morphology, strongly depend on the parameters of the adhesion potential, h_0 and γ. For instance, for large values of h_0, the wrinkles are surrounded by regions of negative out-of-plane displacement, Fig. 3.1(d), absent for small h_0, Fig. 3.1(e).

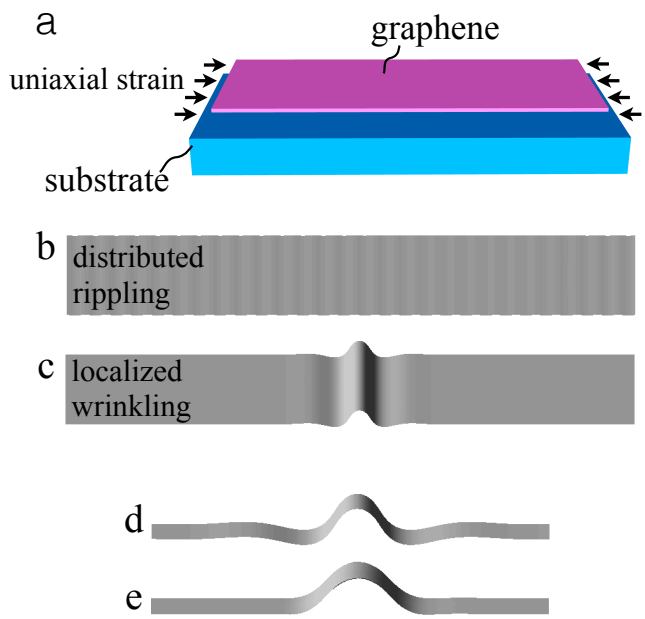

Figure 3.1: A setup of monolayer graphene upon uniaxial compression is presented in (a). Representative simulation of a ripple-to-wrinkle transition of is given in (b, c). The length of the domain along the uniaxial compression is 200 nm, the adhesion energy is 0.45 J/m^2, and equilibrium separation of the potential is 6 nm. A lateral view of the fold is given in (d), to be compared with the fold morphology obtained with a smaller equilibrium separation ($h_0 = 0.6$ nm) shown in (e).

In experiments of supported graphene, distributed ripples associated to compression have not been reported. However, as discussed before by analogy to similar systems, localized wrinkles are presumably preceded by such ripples. One of our goals in the present chapter is to understand the emergence of wrinkles under uniaxial compression, to characterize their spacing, and to examine quantitatively the effect of the mechanical coupling between graphene and the substrate.

1 Emergence of rippling

To understand the emergence of rippling and wrinkling in supported graphene, we develop next a simple analytical model, largely following previous works on compressed thin films (Chen and Hutchinson, 2004; Huang et al., 2005). We consider a rectangular graphene membrane under uniaxial compression. We denote by $u(x)$ and $w(x)$ the in-plane and the out-of-plane displacements of the film, and by ε the uniaxial in-plane strain. The stretching

and bending energies of the film can be computed as

$$U_s = \frac{\bar{Y}}{2}\int_\Omega \varepsilon^2 \, dS, \quad U_b = \frac{D}{2}\int_\Omega w''^2 \, dS, \tag{3.1}$$

where we introduce $\bar{Y} = Y_s/(1-\nu^2)$ to simplify the expressions. To understand small amplitude rippling deformations, we linearize the van der Waals energy as

$$U_v = \frac{27\gamma}{2h_0^2}\int_\Omega w^2 \, dS. \tag{3.2}$$

Adopting a von Karman nonlinear plate theory (Landau and Lifshitz, 1959), the membrane strain of the film can be approximated as

$$\varepsilon = \varepsilon_0 + u' + \frac{1}{2}w'^2, \tag{3.3}$$

where ε_0 represents the globally applied lateral strain on the film. We consider the ansatz $w(x) = A\cos(kx)$ for the out-of-plane displacement. By requiring the uniformity of the in-plane tension or strain, see Equation (3.3), the in-plane displacements should obey $u(x) = (1/8)k^2A^2\sin(2kx)$, and the constant strain becomes $\varepsilon = \varepsilon_0 + (1/4)k^2A^2$ (Huang et al., 2005). We note that the applied strain on the system, here $\varepsilon_0 < 0$, differs from the film membrane strain $\varepsilon < 0$, which is partially relaxed by the positive term $(1/4)k^2A^2$. The stretching energy difference per unit area takes the form

$$\Delta\bar{U}_s(A,k) = \frac{\bar{Y}}{2}\left(\varepsilon^2 - \varepsilon_0^2\right) = \frac{T_0}{4}k^2A^2 + \frac{\bar{Y}}{32}k^4A^4, \tag{3.4}$$

where $T_0 = \bar{Y}\varepsilon_0$ is a reference surface tension (it is only the actual surface tension for a uniform planar state). The total energy difference per unit area then becomes

$$\Delta\bar{U}(A,k) = \left(\frac{T_0}{4}k^2 + \frac{D}{4}k^4 + \frac{27\gamma}{4h_0^2}\right)A^2 + \frac{\bar{Y}}{32}k^4A^4, \tag{3.5}$$

where the last term accounts for the stretching induced by wrinkling, and has a stabilizing effect.

The onset of rippling from the planar state ($A = 0$) can be established by the loss of

stability condition $\partial^2 \Delta\bar{U}/\partial A^2(0,k) \leq 0$, which leads to

$$T_0 \leq -Dk^2 - \frac{27\gamma}{h_0^2 k^2}. \tag{3.6}$$

The wavenumber of the most unstable mode can be found by maximizing the expression above (recall T_0 is negative) with respect to k^2, yielding

$$k = \left(\frac{27\gamma}{h_0^2 D}\right)^{1/4}. \tag{3.7}$$

This expression shows that the finite wave number is set by a competition between bending, which favors long wavelength out-of-plane disturbances, and interaction energy, which favors short wavelength disturbances. Replacing Equation (3.7) and into Equation (3.6), we obtain the critical tension and strain for buckling

$$T_{cr} = -\frac{2}{h_0}\sqrt{27\gamma D}, \quad \varepsilon_{cr} = -\frac{2}{h_0 \bar{Y}}\sqrt{27\gamma D}. \tag{3.8}$$

Minimizing the total energy density in Equation (3.5) with respect to A, we find

$$A = 2\sqrt{-\frac{1}{\bar{Y}}\left(T_0 k^{-2} + D + \frac{27\gamma}{h_0^2}k^{-4}\right)}. \tag{3.9}$$

The expression under the square root is positive beyond the stability point, c.f. Equation (3.6). Replacing the expression above in $\Delta\bar{U}(A,k)$ results in

$$\Delta\bar{U}(k) = -\frac{1}{2\bar{Y}}\left(T_0 + Dk^2 + \frac{27\gamma}{h_0^2}k^{-2}\right)^2. \tag{3.10}$$

Minimizing the energy with respect to the wave number, we recover Equation (3.7) even beyond the critical strain, and obtain

$$\Delta\bar{U}_{min} = -\frac{1}{2\bar{Y}}\left(T_0 + 2\sqrt{\frac{27\gamma D}{h_0^2}}\right)^2. \tag{3.11}$$

Replacing Equation (3.7) into Equation (3.9), we find

$$A = \frac{\lambda}{\pi}\sqrt{(T_{cr} - T_0)/\bar{Y}} = \frac{\lambda}{\pi}\sqrt{\varepsilon_{cr} - \varepsilon_0}, \tag{3.12}$$

where $\lambda = 2\pi/k$ is the wavelength. We shall compare later these estimates with our fully nonlinear simulations.

2 Ripple to wrinkle transition

Similarly to the previous treatment of rippling, we adopt the von Karman theory with an ansatz for the wrinkling geometry in agreement with our simulations. We consider

$$w(x) = A\cos\frac{\pi x}{l} + B\cos\frac{2\pi x}{l} + A - B \tag{3.13}$$

for $x \in [-l, l]$ and $w(x) = 0$ otherwise, for $x \in (-L/2, -l) \cup (l, L/2)$. Here, A and B are amplitudes, l is half of the fold length, and L is the length of the graphene film. The term multiplied by A describes the main feature of the wrinkle, while that multiplied by B models the lateral depressions observed in wrinkles with soft interaction potentials. As the wrinkle breaks the translational symmetry, the length of the domain plays a role now. We demand that the membrane tension (strain) be uniform, see Equation (3.3), and solve for the in-plane displacement from $u'' = -w'w''$. After imposing symmetry, we obtain $u(x) = \hat{u}(x) + \bar{\varepsilon}x$, where

$$\begin{aligned}\hat{u}(x) =& \frac{\pi}{l}\left(\frac{A^2}{8}\sin\frac{2\pi x}{l} + \frac{AB}{3}\sin\frac{3\pi x}{l} - AB\sin\frac{\pi x}{l}\right.\\ &\left. + \frac{B^2}{4}\sin\frac{4\pi x}{l} - \pi\frac{A^2+4B^2}{4}\frac{x}{l}\right)\end{aligned} \tag{3.14}$$

in the interval $[-l, l]$. It is easy to see from Equation (3.3) that in this interval $\varepsilon = \varepsilon_0 + \bar{\varepsilon}$. Outside this interval, graphene remains planar with the same constant strain ε. To find $\bar{\varepsilon}$, we impose continuity of the in-plane displacement at $x = \pm l$, i.e.

$$u(\pm l) = \mp(L/2 - l)\bar{\varepsilon}, \tag{3.15}$$

from which we obtain

$$\bar{\varepsilon} = \frac{\pi^2}{2Ll}(A^2 + 4B^2). \tag{3.16}$$

Thus, the stretching energy difference per unit area becomes

$$\Delta\bar{U}_s(A,B,l) = T_0\bar{\varepsilon} + \frac{\bar{Y}}{2}\bar{\varepsilon}^2. \tag{3.17}$$

A simple calculation shows that the bending energy density can be computed as

$$\bar{U}_b(A,B,l) = \frac{D\pi^4}{2Ll^3}(A^2 + 16B^2) \tag{3.18}$$

We turn now to the graphene-substrate interaction. A harmonic approximation disregards the physics of wrinkling, which is promoted by decohesion for large amplitude out-of-plane displacements of the film, beyond the inflection point of the potential. Also, the wrinkling geometry is strongly affected by the stiffening of the interaction as the film is brought closer to the substrate. With a harmonic approximation, localized wrinkling is never energetically preferable to rippling, from which we conclude that the nonlinearity of the graphene-substrate interaction is crucial to explain the ripple-to-wrinkle transition in this system. We find that the qualitative features of the ripple-to-wrinkle transition can be captured with a third order expansion of the interaction potential. However, for accurate predictions of the model, we approximate the interaction potential with a five term expansion

$$\mathcal{V}(w) = \gamma\bigg(-1 + \frac{27w^2}{2h_0^2} - \frac{135w^3}{2h_0^3} + 225\frac{w^4}{h_0^4} - 612\frac{w^5}{h_0^5} + 957.96\frac{w^6}{h_0^6}\bigg), \tag{3.19}$$

where the last term is modified to match the inflection point of the original potential. The corresponding energy density after integration is

$$\begin{aligned}\bar{U}_v(A,B,l) =& \frac{27\gamma l}{2h_0^2L}(3A^2 - 4AB + 3B^2) - \frac{135\gamma l}{4h_0^3L}(10A^3 - 15A^2B + 18AB^2 - 10B^3) + \\ & \frac{225\gamma l}{4h_0^4L}(35A^4 - 56A^3B + 84A^2B^2 - 80AB^3 + 35B^4) - \\ & \frac{153\gamma l}{h_0^5L}(63A^5 - 105A^4B + 180A^3B^2 - 225A^2B^3 + 175AB^4 - 63B^5) + \\ & \frac{59.87\gamma l}{h_0^6L}(462A^6 - 792A^5B + 1485A^4B^2 - \\ & 2200A^3B^3 + 2310A^2B^4 - 1512AB^5 + 462B^6).\end{aligned} \tag{3.20}$$

The total energy density relative to a planar state under a strain ε_0 is

$$\Delta\bar{U}(A, B, l) = \Delta\bar{U}_s + \bar{U}_b + \bar{U}_v. \tag{3.21}$$

We find candidate equilibrium states by minimizing the total energy with respect to A, B, and l numerically. Depending on the applied strain, ε_0, we estimate the ripple-to-wrinkle transition by comparing the energies of the optimal rippling pattern and of the optimal wrinkle, as reported in the results section.

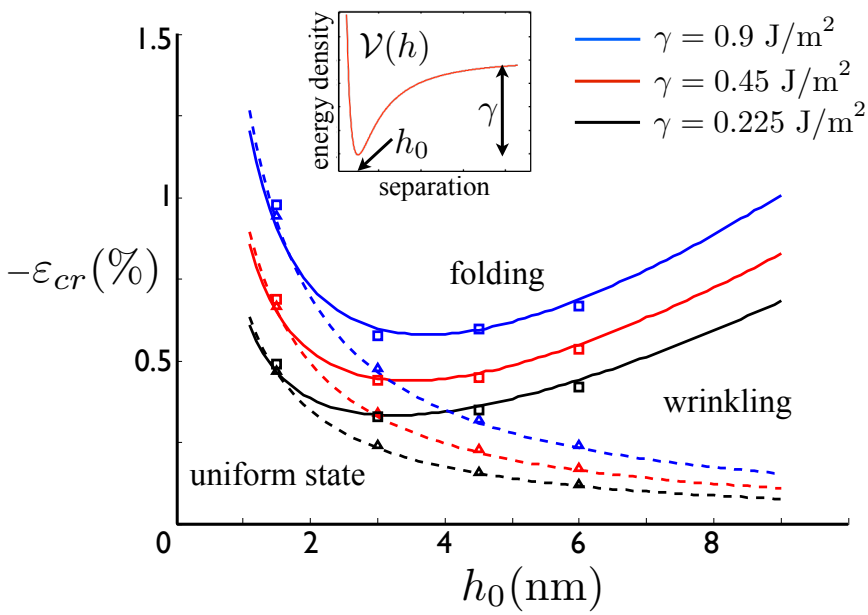

Figure 3.2: Critical strains for the onset of rippling and the ripple-to-wrinkle transition under uniaxial compression, for different van der Waals parameters and for a graphene film of length $L = 200$ nm. Comparisons between analytical model (lines) and numerical simulations (symbols) for both wrinkling (dashed lines, triangles) and ripple-to-wrinkle (solid lines, squares) strains as a function of the equilibrium spacing of the interaction potential h_0, and the adhesion energy γ (different colors). The inset shows the features of the interaction potential.

To check the consistency between the simulations and the theoretical model, we examine in Fig. 3.2 the systematic dependence of rippling and wrinkling on the interaction parameters γ and h_0. Here, we fix L and leave the effect of friction for later. The rippling strain is estimated by Equation (3.8) and the ripple-to-wrinkle strain by energy comparison. The theoretical model predictions (solid and dashed lines) are compared with simulations (sym-

bols), obtaining an excellent agreement throughout the parameter space. In the simulations, we observe that wrinkling is always preceded by rippling. For small values of h_0, the gap between these two strains becomes very small, and therefore, wrinkling appears to bifurcate directly from the planar state. The theoretical model for wrinkling is not very accurate for small h_0. In this regime, even at the onset of wrinkling, the film deviation is significant and reaches beyond the point where the Taylor series expansion of the potential is accurate. While the critical rippling strain exhibits a monotonic decrease as a function of h_0, the ripple-to-wrinkle strain attains a minimum for a finite equilibrium separation, which results in a broader rippling regime as h_0 becomes larger. As mentioned previously, the strain gap between the onset of rippling and the ripple-to-wrinkle transition decreases as L increases. Not surprisingly, the critical strains increase with adhesion energy.

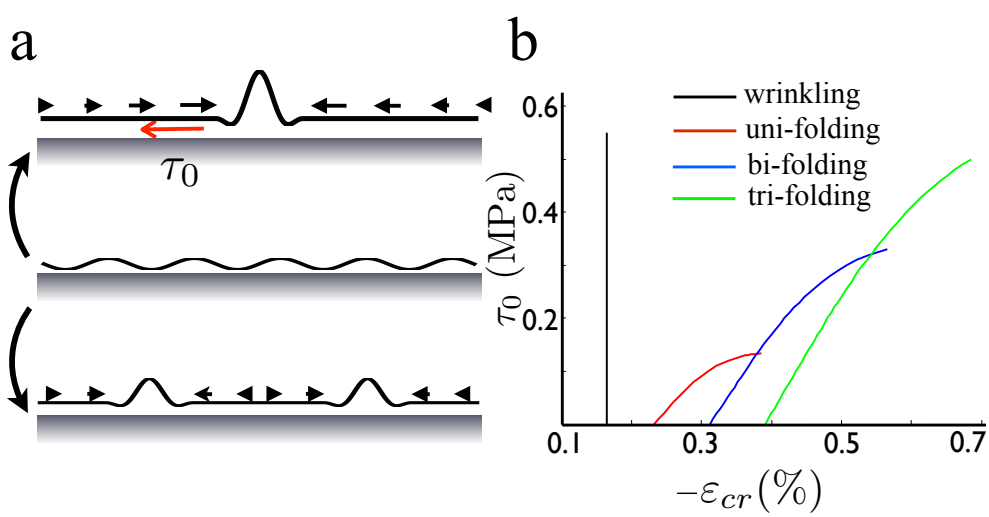

Figure 3.3: Illustration of the sliding of graphene as the system transits from rippling, with distributed excess graphene area relative to substrate area, to wrinkling, with localized excess area (a). Critical strain for rippling and for the transition from rippling to multiple wrinkles as a function of the frictional parameter τ_0, for a uniaxially compressed graphene sheet of length $L = 1$ μm (b).

3 Separation between wrinkles: the role of friction

In the previous model for wrinkling, the length of the graphene film L, which can be interpreted as the separation between wrinkles, has been kept fixed. It is not possible to consider it as an unknown and minimize the total energy density with respect to L as well because

it appears in the denominator of all the terms, see Eqs. (3.17, 3.18, 3.20), and therefore the optimal separation tends to infinity. Physically, we hypothesize that the separation is set by frictional forces between graphene and its substrate. Frictional forces in graphene and carbon nanotubes have been measured in other contexts (Bourlon et al., 2004; Lee et al., 2010).

The model of friction in the simulation has been discussed in Chapt. 2. Let us discuss now the treatment of friction in the analytical model. Since wrinkling requires significant sliding of the graphene sheet relative to the substrate in a large fraction of the sample, see Figure 3.3(a) for an illustration, we assume that the whole surface undergoes sliding, which results in a simple expression for the work of dry friction

$$W_f = \int_\Omega \tau_0 |u| \; dS = \frac{1}{4} \tau_0 \varepsilon_0 L^2 H, \tag{3.22}$$

where H is the width of the sample. To systematically explore the separation, we consider a single wrinkle in a sample of length L, and minimize the energy deviation per unit surface

$$\Delta\bar{U}(A, B, l, L) = \Delta\bar{U}_s + \bar{U}_b + \bar{U}_v + \frac{1}{4}\tau_0 \varepsilon_0 L \tag{3.23}$$

with respect to all its arguments. Since the last term is an increasing function of L while the other terms are decreasing functions of L, this energy leads to a finite separation between wrinkles.

Indeed, as illustrated in Fig. 3.3(a), transitioning from a rippled state to a wrinkled state requires sliding of the graphene sheet relative to the substrate, as the uniformly distributed excess area of a rippled configuration is brought to a localized wrinkle. For a given applied strain, wrinkles separated by a large distance are energetically favorable as compared to smaller wrinkles closer to each other, but dissipate a larger frictional work. Thus, a competition between potential energy (elastic and adhesion) and frictional work is established. The tribological properties of supported graphene have been examined experimentally with AFM (Lee et al., 2010). The frictional traction between different shells in multi-walled carbon nanotubes has been reported to be in the range $\tau_0 = 0.2$ to 0.85 MPa (Cumings and Zettl, 2000; Yu et al., 2000; Bourlon et al., 2004), while τ_0 between graphene and polyethylene terephthalate (PET) has been found to range between 0.46 to 0.69 MPa (Jiang et al., 2013). These experiments probe a similar situation as that studied here, where the normal

force confining the sliding surfaces is not externally applied but rather due to their cohesion. Also, friction can be presumably controlled by the chemistry and topography of the substrate surface.

Figure 3.3(b) shows the critical rippling strain together with the critical strain for forming one, two, or three wrinkles, as a function of the frictional parameter τ_0 (the maximum shear traction that the substrate can exert on the graphene sheet) for a sheet of length $L = 1$ μm. The adhesion parameters are $\gamma = 0.45$ J/m^2 and $h_0 = 4.5$ nm. We assume that rippling results in negligibly small tangental displacement, and thus the rippling strain is independent of τ_0. In the absence of friction, the figure shows that configurations with a single wrinkle are preferred. However, the work of friction affects in a different way the uni-, bi-, and tri-wrinkling configurations, and for larger τ_0, two or three wrinkles become favorable.

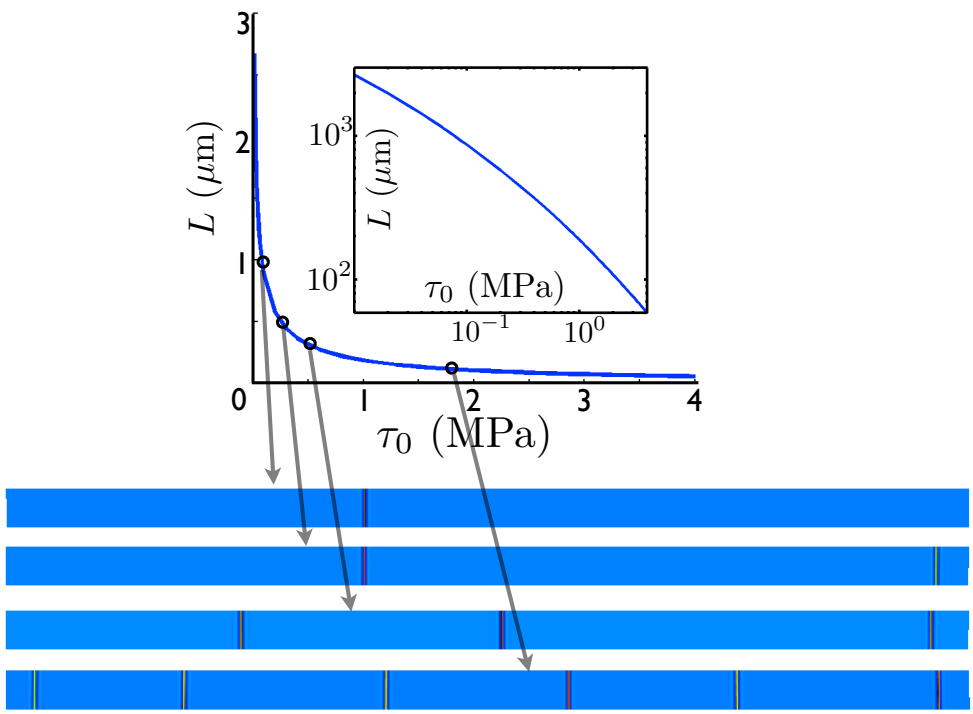

Figure 3.4: Separation between wrinkles L as a function of the friction parameter τ_0 predicted by the theoretical model (top), checked against the simulations for four selected frictional coefficients (bottom). The color represents the out-of-plane deviation $w(x)$. The inset shows L as a function of τ_0 in a log-log scale, to highlight the fact that the relation is not a power-law.

We examine the systematic dependence of the wrinkle separation as a function of fric-

tional coefficient τ_0 in Fig. 3.4, where we minimize the potential energy and frictional work in Equation (3.23) with respect to L as well. We test the theoretical model predictions against simulations for four selected values of τ_0, and find they are in a very good agreement.

Contributions

We summarize here the most significant contributions of this work, which has been published as a research paper in (Zhang and Arroyo, 2013):

1. we study the emergence of spontaneous wrinkling in supported and laterally strained graphene with high-fidelity simulations based on an atomistic-informed continuum model.

2. We theoretically analyze the ripple-to-wrinkle transition of supported graphene under the uniaxial compression. We characterize the onset of buckling and the nonlinear behavior after the linear instability in terms of the adhesion and frictional material parameters of the graphene-substrate interface.

3. We find that localized wrinkles evolve from a distributed rippling linear instability due to the nonlinearity in the van der Waals graphene-substrate interactions.

4. When graphene sample is supported on a tight substrate, e.g. silicon-oxide and upon compression, localized wrinkles are transited from planar surface without an observable rippling stage, which has been proved by experiments.

5. We identify friction as a selection mechanism for the separation between wrinkles, as the formation of far apart wrinkles is penalized by the work of friction. We quantitively study the separation distance between wrinkles in terms of the interfacial shear strength in the interface (friction) theoretically and by simulations.

Chapter 4

Spontaneous wrinkling upon biaxial compression

Having understood the emergence of wrinkling under uniaxial compression, we turn now to the much more complex case of biaxial compression. Here, the boundary conditions are incompatible with inextensible deformations, which in the case of unsupported crumpling of thin elastic films has been shown to lead to complex and localized deformation patterns (Witten, 2007).

1 Spontaneous wrinkling under isotropic compression

We first examine the spontaneous emergence of localized wrinkles upon isotropic biaxial compression, see Fig. 4.1(a). Beyond a threshold strain, the system departs from a planar state and develops a distributed, small-amplitude rippling instability throughout the sample ($\varepsilon_c = 0.6\%$), but since it produces polarized plane-wave deformations and strain is isotropic, many domains with random orientations develop, similar to labyrinth patterns previously reported in other compressed thin films (Huang et al., 2005). Upon further compression ($\varepsilon_c = 1.2\%$), the out-of-plane deformation localizes into short wrinkles, which partially release rippling in their vicinity. Localization is caused by the decohesion of the graphene-substrate interaction. Ripple and wrinkle coexistence has been reported in CVD graphene samples (Liu et al., 2012). As compressive strain increases, wrinkles grow and connect to form a network partitioning the sample into nearly flat subdomains. During this reorgani-

zation, most ripples and some wrinkles disappear, and the network simplifies by aligning and merging neighboring wrinkles that were previously along similar directions ($\varepsilon_c = 2.4\%$). While wrinkles can form complex structures where they meet, the abundance of simple T-junctions is noteworthy. Once the wrinkle network has matured, further compression increases the wrinkle height without significant reorganization. The equilibrium separation chosen here is relatively large to better visualize the competition between distributed rippling and localized wrinkling, which results in a compliant interaction since the stiffness of the adhesion potential is proportional to γ/h_0^2. For very tight interaction as in atomically flat substrates, e.g. h_0 below 1 nm, the system withstands larger strains before buckling and then abruptly transits to wrinkling after an almost unnoticeable rippling regime. The ripple-to-wrinkle transition reported here is reminiscent of that observed in other elastic sheets coupled to different substrates (Pocivavsek et al., 2008; Zang et al., 2012; Kim et al., 2011).

2 Modulating wrinkle patterns through friction and strain anisotropy

Spontaneous wrinkling can be modulated in various ways. Since the emergence of wrinkling requires significant sliding of graphene relative to the substrate, frictional forces determine the expected separation between wrinkles (Zhang and Arroyo, 2013). By considering a significantly larger interfacial shear strength in Fig. 4.1(b), many more short wrinkles nucleate and the reorganization of the wrinkle network is hindered, leading to smaller subdomains. Friction could be modulated experimentally by controlling the pressure difference across the graphene sheet (Kitt et al., 2013; Pugno et al., 2013), since graphene is impermeable to common gases (Bunch et al., 2008). On the other hand, strain anisotropy leads to ripples and wrinkles aligned with the principal directions of anisotropy (Huang et al., 2005; Kim et al., 2011), see Fig. 4.1(c). The similarity between the isotropic (Li et al., 2009; Robertson et al., 2011; Obraztsov et al., 2007; Calado et al., 2012; Liu et al., 2012) and anisotropic (Zhu et al., 2012; Liu et al., 2012) wrinkle patterns observed in supported single and few-layer graphene and those obtained here is remarkable.

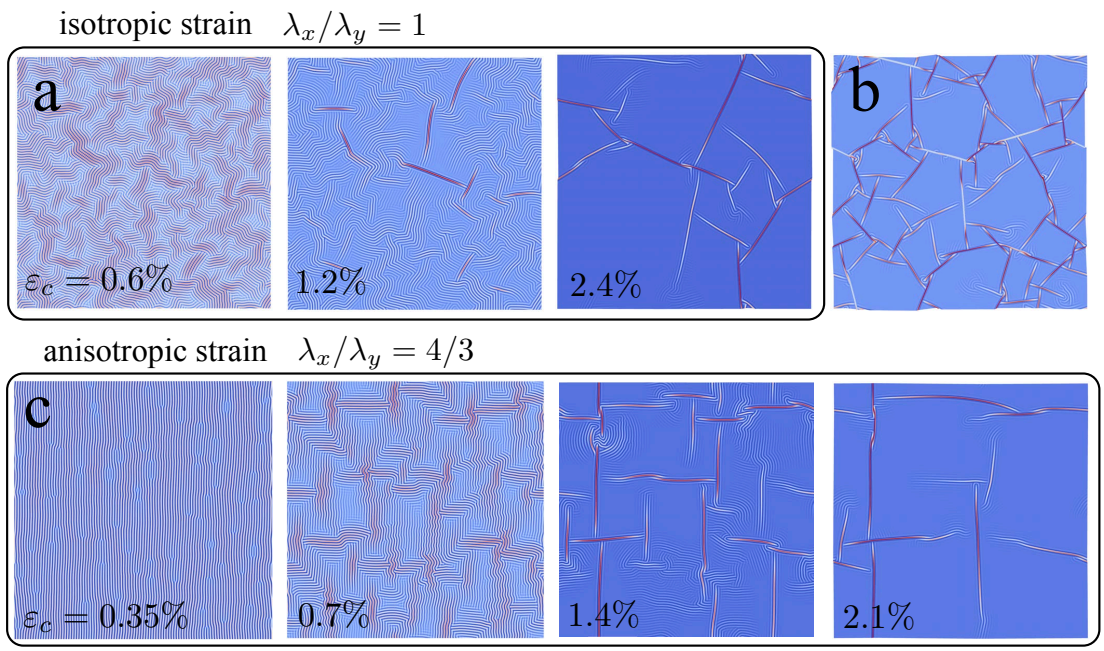

Figure 4.1: Spontaneous wrinkling under biaxial compression. (a) Morphological evolution of the buckling pattern of supported graphene upon isotropic biaxial strain (500 nm × 500 nm sample, $\tau_0 = 0.3$ MPa, $h_0 = 4.5$ nm, $\gamma = 0.45$ J/m^2). The blue-to-red color maps represent the out-of-plane displacement, and the color scale is chosen in each case to better highlight the deformation pattern. The maximum out-of-plane displacement ranges from 0.2 nm at $\varepsilon_c = 0.6\%$ to 3 nm at $\varepsilon_c = 2.4\%$. (b) A denser pattern of wrinkles is obtained with higher friction ($\tau_0 = 1.8$ MPa). (c) Under anisotropic compression, ripples and wrinkles align with the principal directions of strain.

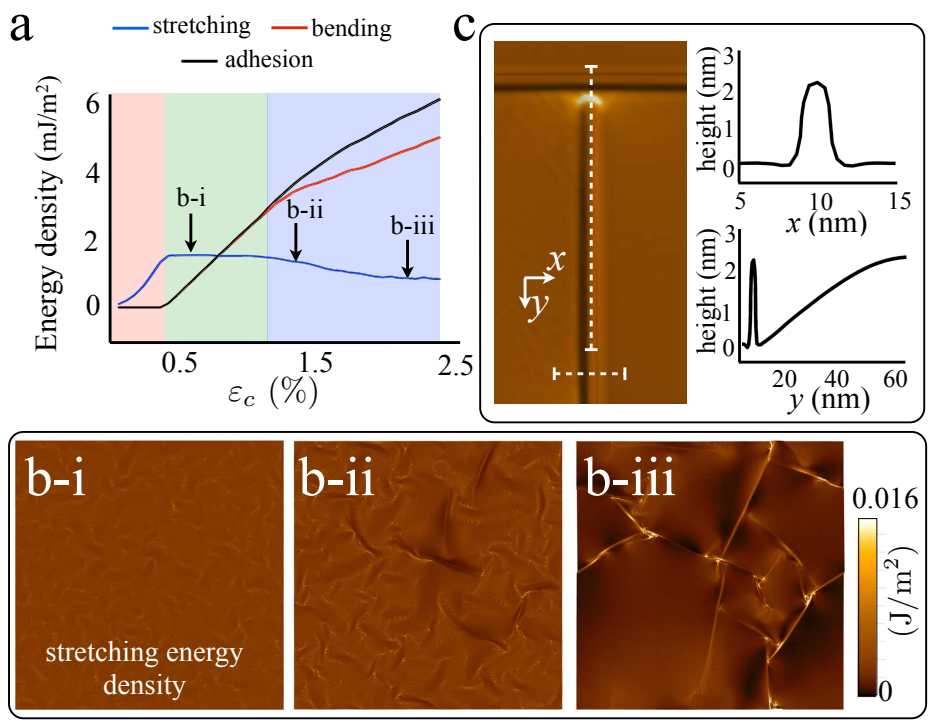

Figure 4.2: Energetics of spontaneous wrinkling. (a) Different components of the energy density as a function of compressive strain, where the planar (red), rippled (green) and wrinkled (blue) stages have been shaded. (b) Maps of stretching energy density corresponding to the snapshots in Fig. 4.1(a). (a) and (b) depict wrinkling as a process of relaxation and focusing of stretching energy. (c) Geometry and stretching energy density of a T-junction. Along the y direction, one of the wrinkles very slowly decreases its amplitude as it approaches the other wrinkle, remaining nearly developable. However, in a very small region at the tip of the vanishing wrinkle, a very strong focusing of Gaussian curvature and stretching energy can be observed.

3 Energetics and the role of stretching

To better understand the mechanics leading to these wrinkle networks, we analyze next the energetics of the process. Fig. 4.2(a) shows different components of the energy (stretching, bending and adhesion) per unit area as a function of compressive strain. While the sample remains planar and at its equilibrium separation (red-shaded region), the stretching energy is the only contribution, and it grows quadratically as expected for an elastic material under small deformation. At a critical strain, it is energetically favorable to further accommodate compressive strain by distributed rippling. This out-of-plane deformation upsets the bending and adhesion energies, which linearly increase, but keeps stretching energy constant (green-shaded region). The competition between adhesion and bending energy sets the rippling wavelength. The figure shows that, beyond a second threshold, localized wrinkling further relaxes the energy; bending and adhesion energies grow at a slower rate, and stretching energy progressively reduces. This response under biaxial compression is very different from the wrinkling behavior under uniaxial compression, where stretching energy reduces towards zero much faster. Here, it is not possible to accommodate biaxial compression without significant stretching, which becomes a key factor in understanding wrinkle networks and the junctions they form.

Unlike bending deformations, in-plane stretching cannot be directly visualized from the out-of-plane displacement maps. For this reason, we show in Fig. 4.2(b) the spatial distributions of stretching energy during the process. While in the rippling stage (b-i) the stretching energy is quite uniformly distributed, it progressively relaxes around the nascent wrinkles (b-ii). When the wrinkle network is fully formed (b-iii), the contrast in stretching energy distribution dramatically increases, by nearly relaxing in most of the sample and strongly focusing it along some wrinkles and mainly at wrinkle junctions and other network point defects. Thus, wrinkling can be understood as a process of stretching energy relaxation and focusing, at the expense of bending and adhesion energy.

The relation between sheet morphology and stretching can be understood from Gauss Theorema Egregium, which implies that doubly-curved (non-developable) regions of the film are necessarily stretched, while developable straight wrinkles can exist without stretching (Witten, 2007). Junctions involve localized double curvature, which explains why stretching focuses at points, while bending and decohesion also concentrate along the linear singly-curved wrinkles. Amongst the diversity of junction morphologies, T-junctions appear to be

stable low-energy configurations, see Fig. 4.2(c). Interestingly, T-junctions are frequently observed in supported graphene (Liu et al., 2012). In the context of crumpling of unsupported thin elastic sheets including graphene, focusing of stretching energy at point (developable cones) and line (stretching ridges) deformation features has been extensively studied (Cerda et al., 1999; Witten, 2007; Pereira et al., 2010). T-junctions between wrinkles seem to be an analogous building block for compressed and adhered sheets (Aoyanagi et al., 2010).

4 Reproducibility of wrinkle patterns

We examine next the sensitivity of the computational result to key numerical parameters: mesh refinement, load increment size, and dimensions of the periodic domain. We performed many simulations varying these parameters within the computationally feasible range, some of which are reported in Fig. 5.1. We found that the precise location of wrinkles is completely different when the load increment size or the dimensions of the periodic box are changed (Fig. 5.1(a)). This variability is a consequence of the massive non-uniqueness of equilibrium states in the system. However, the general features of the pattern, in terms of wrinkle spacing and orientations, are similar. More quantitatively, as shown by the evolution of the different energy components as a function of strain in Fig. 5.1(b), the numerical equilibria for different computational parameters exhibit very similar global behavior. Our simulations appear to be converged in terms of the periodic domain and mesh size, and the most noticeable differences are observed for large load steps, with a delayed ripple to wrinkle transition, presumably due to an inaccurate estimation of the work of friction. In summary, given the fundamental metastability of buckling in highly symmetric systems, the precise wrinkle pattern is highly dependent on details about numerical parameters, but the global characteristics of the solutions are remarkably insensitive.

Contributions

We summarize here the most significant contributions of this work, which has been published as a research paper in (Zhang and Arroyo, 2014):

1. We have reproduced computationally the most salient features of wrinkle networks observed in supported graphene.

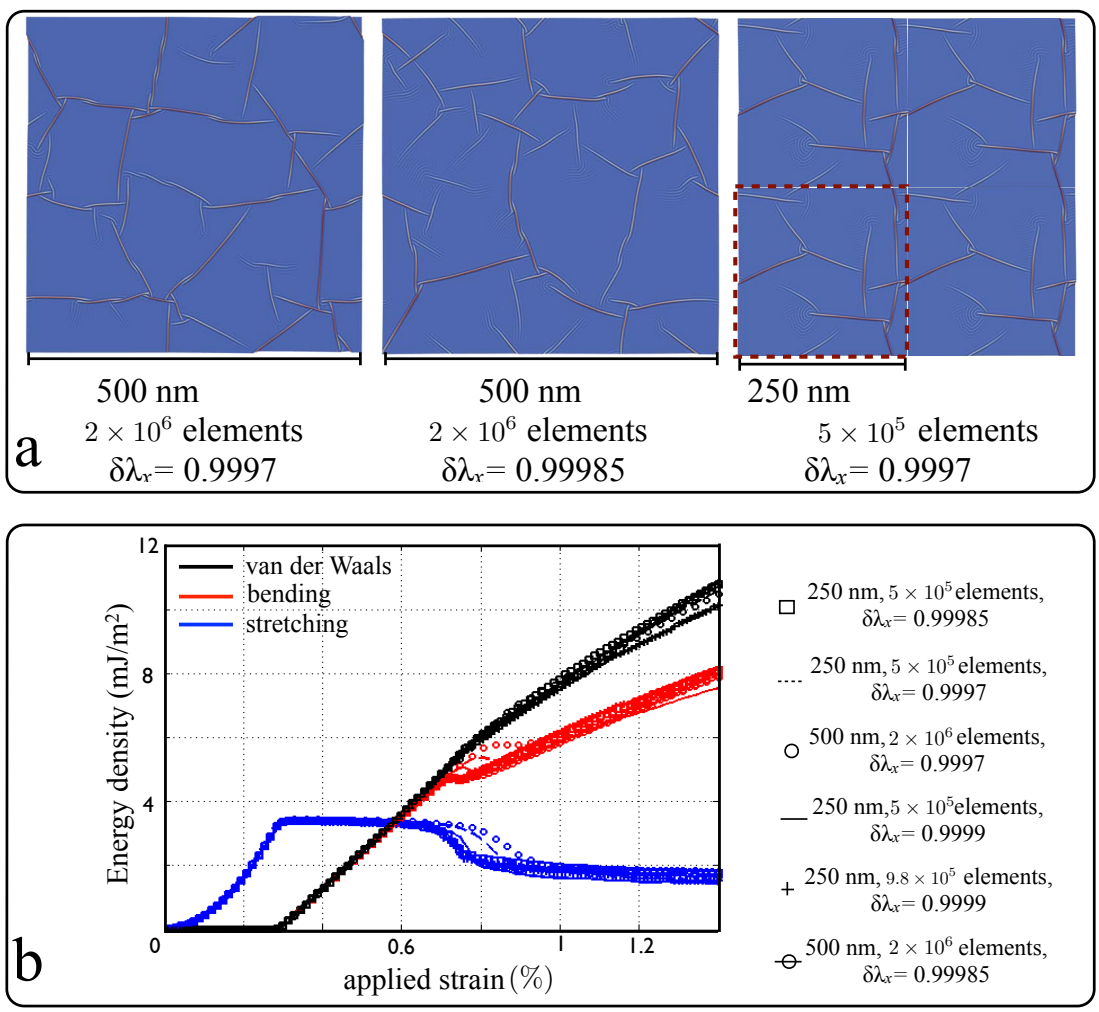

Figure 4.3: Wrinkling pattern (a) and different contributions to the energy of the system as a function of applied strain (b), as the key numerical parameters—mesh size, load increment size, and dimensions of the periodic domain—are varied. In all the simulations, $\tau_0 = 1.8$ MPa, $h_0 = 1.5$ nm, $\gamma = 0.45$ J/m^2.

2. We have identified the influence of strain anisotropy and the adhesive and frictional properties on the morphology of spontaneously-formed wrinkle networks.

3. We have analyzed the energetics of the process. Wrinkling can be understood as a process of stretching energy relaxation and focusing on the junctions. T-junctions are frequently observed and energetically favorable.

4. Our simulations illustrate the fundamental difficulty in trying to control wrinkle networks by compressing supported elastic thin films.

Chapter 5

Control of strain-engineered wrinkle networks in supported graphene

With the understanding of the mechanics of spontaneous wrinkling in Chap. 4, we turn now to strategies to precisely control the geometry of the wrinkle network amongst the vast range of available wrinkling pathways. While controlling buckling instabilities is notoriously difficult, particularly under multiaxial compression, there have been different attempts to guide wrinkles in different supported thin films (Hendricks et al., 2010). Wrinkling patterns in metal-capped thin polymer films have been modulated, but not precisely controlled, by chemically patterning the adhesive properties of the substrate (Vandeparre et al., 2007). Wrinkles in supported graphene have been shown to predominantly form at substrate corrugations under uniaxial compression (Kim et al., 2011; Pan et al., 2011; Liu et al., 2012).

1 Controlling wrinkle networks through weak adhesion stripes on the substrate

Building on these ideas, we attempt to conform wrinkles to patterns of stripes of weaker adhesion in an otherwise homogeneous substrate. We model the stripes of weaker adhesion by spatially modulating the adhesion energy as $\gamma(x,y) = \bar{\gamma}\left\{1 - \exp\left[-dist(x,y;\ell)^2/c^2\right]\right\}$, where γ is the adhesion energy between graphene and substrate (see Chap. 2), and $dist(x,y;\ell)$

denotes the distance of a point to the closest line in the pattern ℓ. We take $c = 1$ nm, which leads to a stripe width of ~ 4 nm. We found that graphene wrinkles tend to follow the width of stripes. However, if the stripe width becomes comparable to $\sqrt{D/\gamma} \approx 0.7$ nm, then bending stiffness can significantly impede the formation of wrinkles conforming to such narrow stripes. In experiment, such patterns may be implemented through physicochemical modification and nanolithography.

We examine first uniaxial compression, where in the absence of stripes the wrinkle separation strongly depends on the frictional properties (Zhang and Arroyo, 2013), see the black curve in Fig. 5.1(a). We expect that the frictional selection principle for wrinkle separation may interfere with our strategy to control the wrinkle location, e.g. uncontrolled wrinkles could form between the stripes for very high friction or some stripes may fail to accommodate a wrinkle for very small friction. To address this question, we uniaxially compress a 1 μm graphene ribbon supported on a substrate decorated with uniformly spaced stripes 4 nm wide and 200 nm apart. Fig. 5.1(a) shows the average wrinkle spacing (red circles) obtained from simulations with different frictional properties. It can be observed that, given a target wrinkle separation, wrinkles conform to stripes in a relatively wide range of interfacial shear strength. Thus, stripes of weak adhesion appear to be a robust method to control wrinkle location if properly tuned to the graphene-substrate friction.

We extend next this idea to two-dimensional isotropic and anisotropic stripe patterns under biaxial loading, see Fig. 5.1(b). For isotropic compression, we attempt an isotropic honeycomb pattern of stripes, and observe that wrinkles can conform to the pattern, forming two types of Y-junctions with broken-symmetry, Fig. 5.1(b-i). Since under anisotropic compression we found that spontaneous wrinkles form along perpendicular directions, we choose a rectangular grid of stripes. We find that wrinkles first form perpendicular to the direction of maximum strain, and then match the target pattern as a second family of wrinkles develops, forming X-junctions with the first family, Fig. 5.1(b-ii). The wrinkle networks robustly conform to the desired patterns for a wide range of parameter values, but the proposed strategy fails if the pattern is not properly tuned the adhesive/frictional properties, or to the compression anisotropy. For instance, X-junctions can become unstable, Fig. 5.1(c), particularly when the two families of perpendicular wrinkles have the same nominal height ($\alpha = 1$). For tight adhesive interactions, e.g. $h_0 = 0.5$ nm representative of graphene on an atomically flat surface, X-junctions become severely strained and kink. For

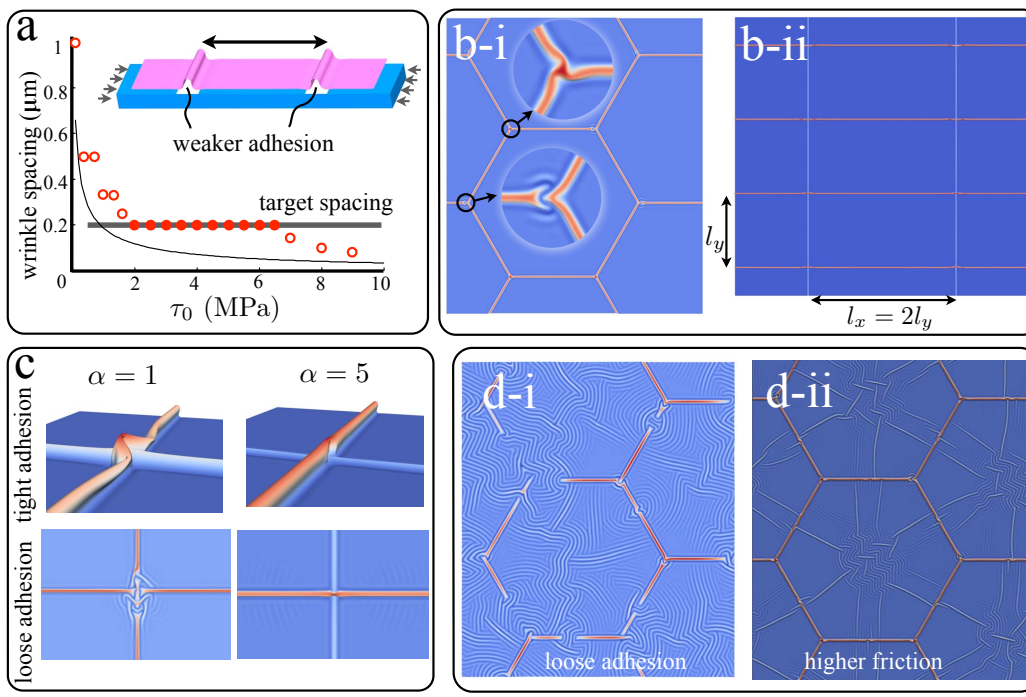

Figure 5.1: Controlling the wrinkle location with stripes of lower adhesion. Under uniaxial compression, (a) shows the average wrinkle spacing as a function of τ_0 (red circles), compared to the target spacing (horizontal gray line) set by the separation between stripes. Simulations where wrinkles conform to the stripes are shown as filled red circles. For very large τ_0, additional wrinkles form between stripes, while for very small τ_0 wrinkles do not form in every stripe. The black curve shows the theoretical wrinkle separation as a function of τ_0 in the absence of stripes. This idea can be extended to two-dimensional wrinkle networks under isotropic (b-i) and anisotropic (b-ii) biaxial loading, if the adhesion is tight enough (here, $h_0 = 1.5$ nm and $\tau_0 = 4$ MPa). $\alpha = l_x\lambda_x/(l_y\lambda_y)$ measures the nominal height ratio between the two sets of wrinkles in the rectangular pattern. As shown in (c), X-junctions become unstable if the nominal height ratio is close to one, by either kinking for tight adhesion or by spreading into a rippled pattern for loose adhesion. X-junctions are stabilized if the nominal height of the kinks is significantly different. (d) shows how the honeycomb pattern fails to form if the adhesion is too loose (d-i) or the friction too high (d-ii).

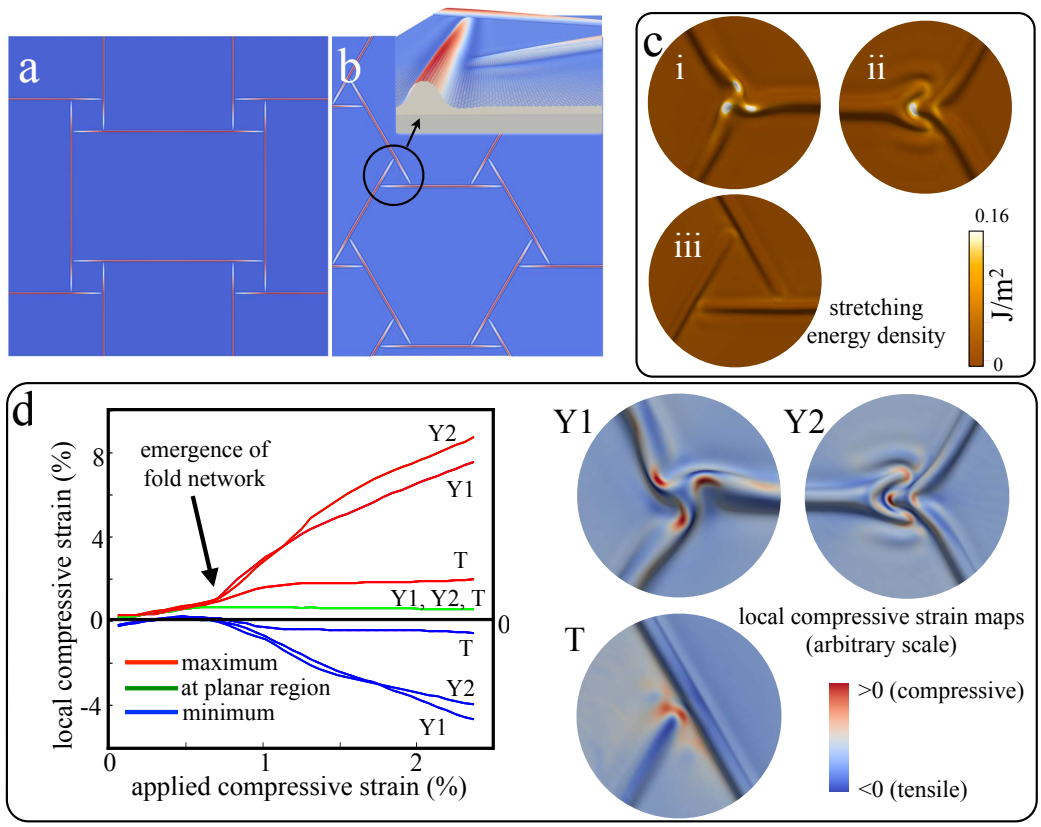

Figure 5.2: Different junctions types and their local strain behavior. (a) and (b) show variations of the rectangular and honeycomb patterns involving only low-energy T-junctions. (c) Stretching energy of the two types of Y-junction in Fig. 5.1(b-i) compared to an analogous connecting structure consisting of three T-junctions in (b), at $\varepsilon_c = 2.4\%$. (d) Local strain behavior of the two types of Y-junctions and a T-junction as a function of applied strain. The color scale for the local compressive strain maps has been chosen in each case to better show the strain distribution.

very loose interactions, e.g. $h_0 = 6$ nm, which may model a soft polymeric substrate, X-junctions destabilize into a complex partially rippled structure. X-junctions can be stabilized by changing the nominal height ratio between the two systems of wrinkles, e.g. $\alpha = 5$ in Fig. 5.1(c). The isotropic honeycomb wrinkle pattern fails to form for loose interactions due to the interference of rippling, Fig. 5.1(d-i). Fig. 5.1(d-ii) shows how an excessive interfacial shear strength relative to the pattern dimensions leads to uncontrolled wrinkles.

Since T-junctions are energetically favorable structures in spontaneous biaxial wrinkling, we turn now to isotropic and anisotropic networks that only exhibit these kinds of junctions, see Fig. 5.2(a,b). We find that for sufficiently tight adhesive interactions (h_0 smaller than ~3

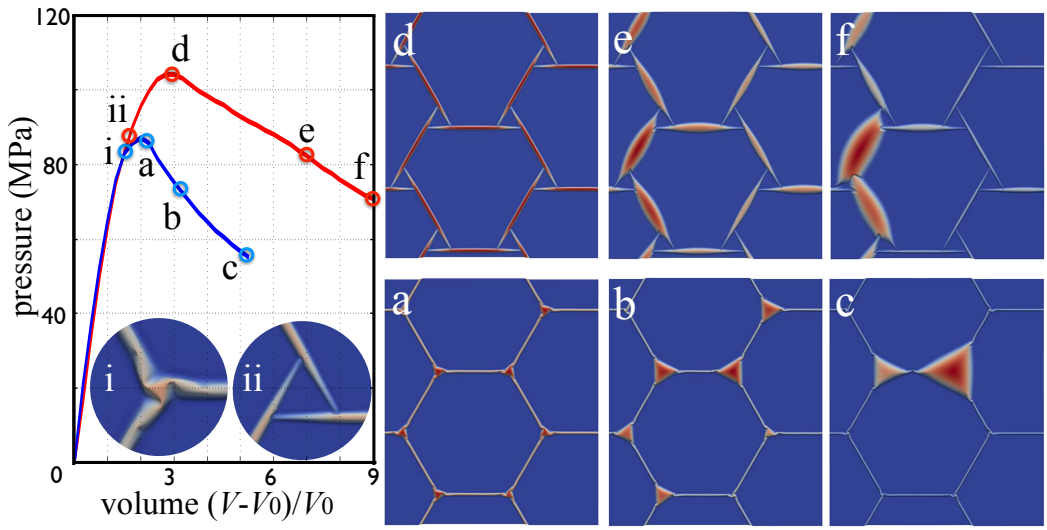

Figure 5.3: Stability of the wrinkle networks under internal pressure caused by an enclosed fluid. (a-c) and (d,e) show snapshots of Y- and T-junction patterns as mass is added into the interstitial space. The left plot shows the pressure-volume relation along this process for the two patterns, where V_0 is the volume enclosed by the wrinkled graphene membrane before pressure is applied.

nm), such patterns form in a very reproducible way, and are not susceptible to instabilities of the junctions. T-junctions are much lower energy configurations as compared to the Y-junctions of the honeycomb lattice, Fig. 5.2(c). Even though T-junctions are attractive due to their stability, other more energetic junctions may be more interesting from a strain engineering viewpoint. Fig. 5.2(d) analyzes how strain is distributed spatially. Local in-plane strain has an areal component and a shear component. We focus on the local compressive strain (local area change) as a function of the applied compressive strain ε_C for two types of Y-junctions (Y1 and Y2) and a T-junction (T). We quantify the spatial non-uniformity of the local strain by tracking its maximum and minimum values, which occur at the junctions, as well as the local strain in the planar region away from wrinkles and junctions. Examining the structure of the strain fields, it can be observed that Y-junctions exhibit complex distributions with strongly localized strain dipoles. Thus, it is possible to create wrinkle networks of diverse geometry and junction configurations, which may attenuate or significantly amplify the applied strain, and hence strain-induced changes in properties, at specific points of the network.

2 Stability of wrinkle networks to interstitial pressure

Along wrinkles, graphene delaminates from the substrate creating nano-channels. Since graphene is impermeable to most gases and liquids (Bunch et al., 2008; Whitby and Quirke, 2007), wrinkle networks could be harnessed as mechanically self-assembled nano-fluidic devices, possibly in combination with existing methods to encapsulate gas underneath supported graphene (Bunch et al., 2008; Koenig et al., 2011; Zabel et al., 2012). Trapped fluid molecules can create a significant pressure difference across a graphene membrane, and therefore it is important to assess the connectivity and stability of the networks of channels under these conditions.

Fig. 5.3 shows the response of two isotropic networks, with Y- and T-junctions, as fluid mass is introduced into the interstitial space until disruption of the network by delamination. We first focus on Y-junctions. As the system becomes pressurized, we observe that all Y2 junctions transform to Y1 junctions. For a wide range of pressures, increasing pressure causes channels to progressively thicken, while maintaining connective junctions, Fig. 5.3(i). Beyond the maximum pressure, further mass input increases the enclosed volume but decreases the pressure as delamination progresses; triangular blisters nucleate at most junctions, and then some expand while others shrink leading to fewer and very large blisters, see Fig. 5.3(a-c). These triangular blisters are remarkably similar to those recently observed (Pan et al., 2012). Networks with T-junctions can also withstand high pressure differences by thickening the wrinkles as pressure increases, see Fig. 5.3(d-f). Our simulations confirm the stability of the fixed mass ensemble beyond the onset of delamination, as observed previously in experiments (Boddeti et al., 2013).

3 Are curved wrinkles stable?

In the previous studies, we examine the possibility of controlling wrinkles by weak adhesion stripes on the substrate. The wrinkle network could be applied as nano-fluidic channels. To enlarge the class of wrinkle networks that can be achieved, we ask ourselves if it is possible to create stable patterns involving curved wrinkles.

A simple straight wrinkle has zero Gaussian curvature, as it is only curved in the direction perpendicular to the wrinkle. However, curved wrinkles are non-developable surface, with curvature along the wrinkle. Gauss Theorema Egregium implies that doubly-curved (non-

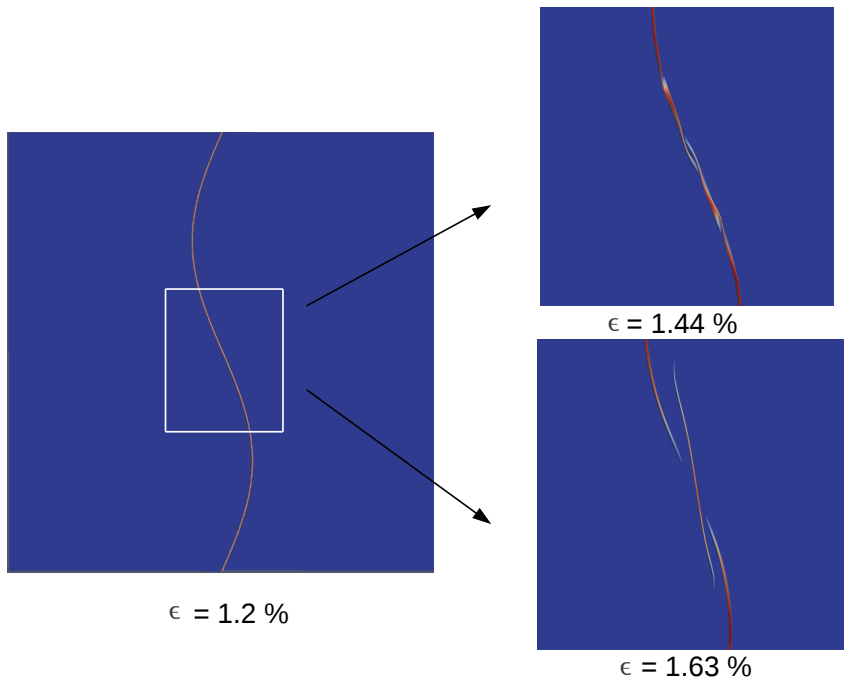

Figure 5.4: A curved wrinkle fragments into wrinkle segments as compressive strain is increased.

developable) regions of the film are necessarily stretched. Our previous simulations have shown that supported graphene tends to develop localized deformations to relax stretching, suggesting that curved wrinkles will only remain stable within a certain range. In research not fully reported here, we have examined this issue. In simulations involving curved weak adhesion stripes, the accumulated stretching energy due to doubly curving competes with bending and adhesion energy, and finally triggers the curved wrinkle fragmentation into wrinkle segments, see Fig. 5.4.

This work confirms the possibility of creating moderately curved wrinkles in supported graphene. As an application in network design, Fig. 5.5 depicts several possible connections by curved wrinkle in designing the wrinkle network.

Contributions

We summarize here the most significant contributions of this work, which has been published as a research paper in (Zhang and Arroyo, 2014):

1. We have proposed a method to precisely control the location of wrinkles through

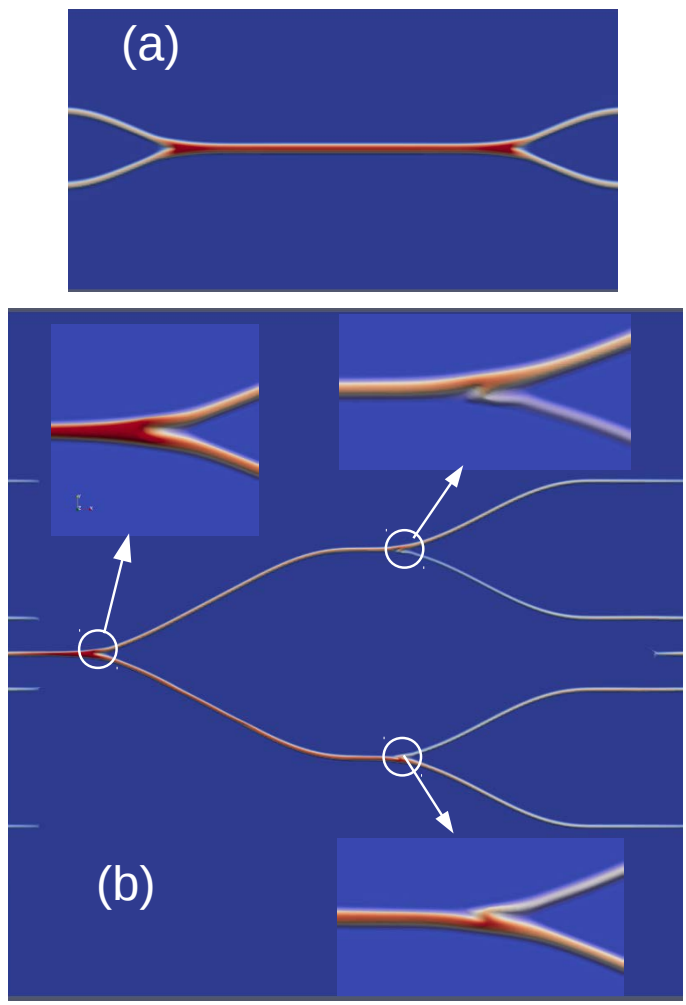

Figure 5.5: (a,b) show an application of curved wrinkles in wrinkle network designing with modified junctions.

patterns of stripes of weaker adhesion on the substrate. For this strategy to succeed, the target pattern has to ben tuned to the graphene-substrate interaction and to strain anisotropy.

2. We have shown that T-junction are very stable and attenuate the applied strain, while Y-junctions are strain amplifiers.

3. We have assessed the connectivity and stability of the networks of channels trapping fluid molecules, opening the door to nano-fluidic applications.

4. We have examined the stability of curved wrinkles.

Chapter 6

Coexistence of wrinkles and blisters in supported graphene

We examine in this chapter the mechanics of bubbles in supported graphene. In experiments, graphene bubbles have been observed with different sizes and shapes. The reported radii of the circular edges of quasi-spherical bubbles range from dozens of nanometers to several microns (Stolyarova et al., 2009; Koenig et al., 2011). Gas released from the substrate can become trapped under the impermeable graphene sample, creating a significant pressure difference across the membrane that produces and stabilizes tense bubbles (Bunch et al., 2008). The amount of gas inside the interstitial space can be used to control the size of bubbles (Koenig et al., 2011; Liu et al., 2013). Moreover, blisters with straight edges have been observed, possibly in association with wrinkles (Pan et al., 2012; Wang et al., 2012). Triangular and quadrangular straight-edged bubbles have been observed and controlled by an external electric field (Georgiou et al., 2011). It has been shown that a small triangular bubble can generate a very large pseudo-magnetic field, demonstrating that the electronic structure of graphene can be strain engineered (Kim and Neto, 2008; Guinea et al., 2010; Levy et al., 2010). Figure 6.1(a-d) shows experimental observations of bubbles of different morphology in supported graphene samples.

The mechanics of quasi-spherical bubbles has been previously examined in detail (Boddeti et al., 2013; Kitt et al., 2013; Yue et al., 2012; Koenig et al., 2011). However, the mechanisms leading to straight-edged bubbles remains unexplored, despite numerous experimental observations. Furthermore, the coexistence and interaction between wrinkles and

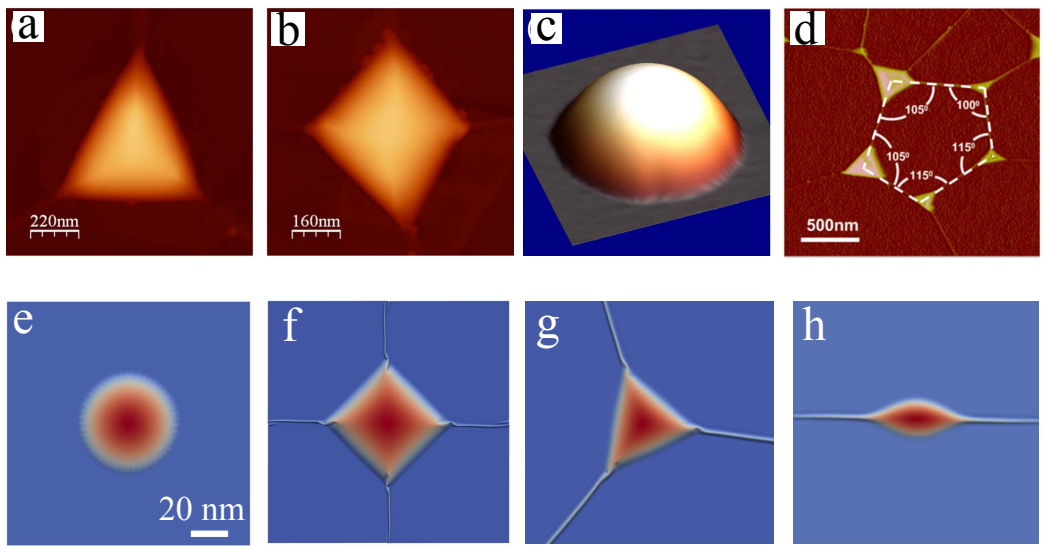

Figure 6.1: (a-c) AFM topography scan of triangular, quadrangular and circular bubbles (Georgiou et al., 2011). (d) A representative AFM image of straight-edged bubbles coexisting with wrinkles (Pan et al., 2012). (e-h) Our simulations on graphene bubbles with various configurations. (e) A circular bubble. (f) A quadrangular straight-edged bubble. (g) A triangular straight-edged bubble. (h) A lenticular bubble. The colormap in (e-h) represents out-of-plane displacement.

blisters has not been investigated. Here, we attempts to address these issues and provide a unified picture of bubbles and wrinkles in supported graphene.

1 Modeling approach

We hypothesize that the shape of bubbles (in particular their circular or straight-edged morphology) and their interaction with wrinkles result from the system trying to adopt energetically favorable configurations for a given compressive strain or amount of interstitial molecules. To test this hypothesis, we consider a simplified set-up with a single and initially circular bubble in equilibrium at the center of a 200×200 nm^2 periodic supported graphene sample. To prepare the system in this state, we artificially weaken the adhesion strength at the center of the sample and gradually increase nRT, in analogy with experiments (Koenig et al., 2011). Once the bubble grows and delaminates from the substrate beyond the weakened region, we remove the adhesion defect and re-equilibrate the system. See Fig. 6.1(e) for a typical stable bubble created with this procedure, which exhibits a circular rim.

Once a circular blister is created, by applying compressive strain (progressively reducing the lateral dimensions of the simulation cell), we observe a variety of straight-edged blisters, associated with wrinkles emanating from the blister's vertices, see Fig. 6.1(f,g). The configurations observed in simulations closely follow those observed in experiments by Pan et al. (2012), see Fig. 6.1(d). In the triangular and quadrangular bubbles reported in Georgiou et al. (2011) Fig. 6.1(a-b), a careful examination also suggests the presence of wrinkles originating at the vertices. We also observe in simulations with anisotropic strain lenticular bubbles, see Fig. 6.1(h). Thus, although the symmetry of our setup favors quadrangular blisters and pairs of wrinkles meeting at a 90° angle, our modeling approach captures some of the salient features of blisters in supported graphene. By focusing on the behavior of a single bubble we analyze in fact a system with a specific density of bubbles given by the lateral dimensions of the periodic box. We will return to this discussion at the end of the chapter.

2 A morphological diagram for bubble/wrinkle coexistence

Based on a systematic set of simulations, see Fig. 6.2(b), we organize our observations in a morphological diagram in the compressive strain-trapped mass (ε_l, nRT) space, see Fig. 6.2(a), where ε_l represents the *linear compressive strain* applied in each direction. To explore this diagram, we start from a circular bubble (white region) and increase ε_l while keeping nRT constant. We observe that short wrinkles nucleate at the periphery of the bubble and gradually elongate until they reach the periodic boundary while the circular bubble transits to a quadrangular straight-edged bubble, see Fig. 6.2(i-iii). At this point, recalling the periodicity of the box, the system adopts a wrinkle network configuration with blisters at wrinkle junctions (light grey region). From this state, we go downward in the diagram by decreasing nRT and observe that the bubble shrinks and finally collapses into a junction connecting the intersecting wrinkles along two orthogonal directions (dark grey region), see Fig. 6.2(v). Moreover, we find that this morphological diagram is largely path-independent. For instance, Fig. 6.2(a) shows with continuous and dashed lines two different paths in (ε_l, nRT) space, which intersect at configurations (iii) and (vi). It can be seen that the equilibrium state depends on the strain and trapped mass, but not on history. As illustrated in the figure, the transitions between different morphologies in the diagram,

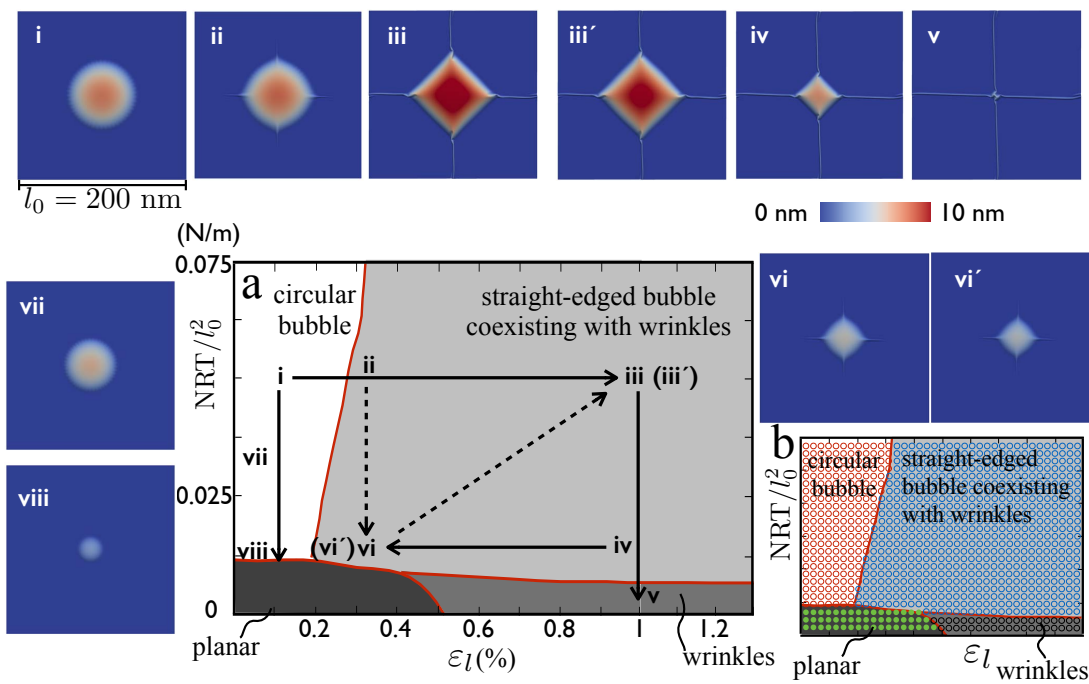

Figure 6.2: A strain-trapped mass morphological diagram of deformations in graphene. (i-iii) depicts the transition from a circular bubble into a straight-edged bubble coexisting with wrinkles, when the biaxially applied compressive strain is increased (ε_l represents the linear applied strain in each direction). Starting from (ii) and decreasing nRT, wrinkles shorten and the bubble becomes small (vi). (iii' and vi') show the same bubble configuration as (iii and vi), but accessed through an alternative path in parameter space. Starting from a straight-edged bubble bubble (iii) and decreasing nRT, the bubble shrinks as a junction connecting two intersected wrinkles (v). (vii and viii) depict shrinking circular bubbles as nRT is decreased from (i). (b) Depiction of the points used to build the morphological diagram, where each state is equilibrated for fixed strain and trapped mass, and qualified according to its morphology.

e.g. from circular bubble to straight-edged bubble coexisting with wrinkles, are gradual. For clarity, we represent them however as sharp lines in Fig. 6.2(a), where the criterion to distinguish between the white and the light grey regions is the nucleation of small wrinkles and the disappearance of small ripples at the periphery of the bubble.

In the circular bubble region, increasing/decreasing nRT results in larger/smaller bubbles, which below a size threshold, become unfavorable compared to the planar configuration (i-vi-viii). Similarly, when compressive strain is reduced in configuration (v), the wrinkle height becomes smaller and at one point, the system transits to the planar configuration.

In fact, once the system gets trapped in the planar state (black region), the morphological diagram is no longer path independent. Indeed, if starting from the planar state we either increase ε_l or nRT, the system stays planar beyond the black region because the planar configuration is metastable with a significant barrier in a broader region. To estimate the region of metastability, we perform a linear stability analysis of the system around the planar state. We first consider the uniformly flat solution for a graphene sheet subjected to ε_c and nRT. The pressure within the interstitial space can be computed from the ideal gas law as

$$p = \frac{nRT}{\bar{h}A_0(1-\varepsilon_l)^2}, \tag{6.1}$$

where $\bar{h}$ is the equilibrium separation and A_0 is initial surface area of the unstrained graphene sheet. The pressure can also be computed from

$$p = \mathcal{V}'(\bar{h}). \tag{6.2}$$

Equating both expressions for p, we obtain an implicit formula for $\bar{h}$, which can be solved numerically given ε_l and nRT. We can then linearize the system around this equilibrium configuration and assess its stability as we did in Section 1 of Chapter 3. In the present situation, the linearized van der Waals potential takes the form

$$\hat{\mathcal{V}} = \frac{\gamma}{2h_0^2}\left[-18\left(\frac{h_0}{\bar{h}}\right)^5 + 45\left(\frac{h_0}{\bar{h}}\right)^{11}\right] w^2, \tag{6.3}$$

which reflects the fact that this potential softens as nRT ($\bar{h}$) increases. Then, recalling our

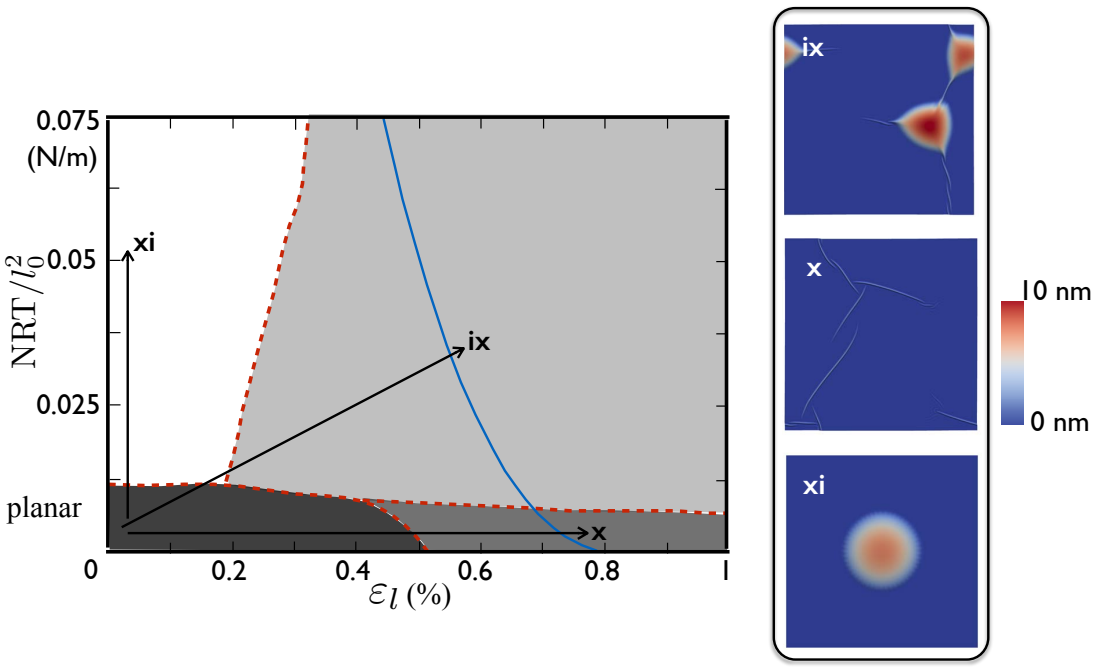

Figure 6.3: Starting from a planar state and increasing both nRT and ε_l, the graphene surface buckles into polygonal bubbles that coexist with wrinkles (ix). With only compressive strain, a planar surface buckles into a network of localized wrinkles (x). (xi) By only increasing nRT, a circular bubble can be formed starting from a small defect on the substrate.

results in Chapter 3, c.f. Equation (3.8), we obtain the critical strain for linear instability

$$\hat{\varepsilon}_{cr} = -\frac{2}{h_0 \bar{Y}} \sqrt{\left[-18\left(\frac{h_0}{\bar{h}}\right)^5 + 45\left(\frac{h_0}{\bar{h}}\right)^{11}\right] \gamma D}. \tag{6.4}$$

This equation allows us to delimit the region of marginal stability of the planar configuration in the morphological diagram as a blue curve in Fig. 6.3. We test with fully nonlinear calculations this boundary for meta-stability of the planar state. Starting at the origin of the diagram, we increase both strain and trapped mass to describe a diagonal path. As predicted by the estimate, we find that the system abruptly transits from the planar state to a state where bubbles coexist with wrinkles when the diagonal path intersects the blue stability boundary. If instead we increase only strain, we find that in agreement with the morphological diagram the system transits to a wrinkled configuration as we reach the marginal stability threshold. If we increase only trapped mass, a circular bubble can be

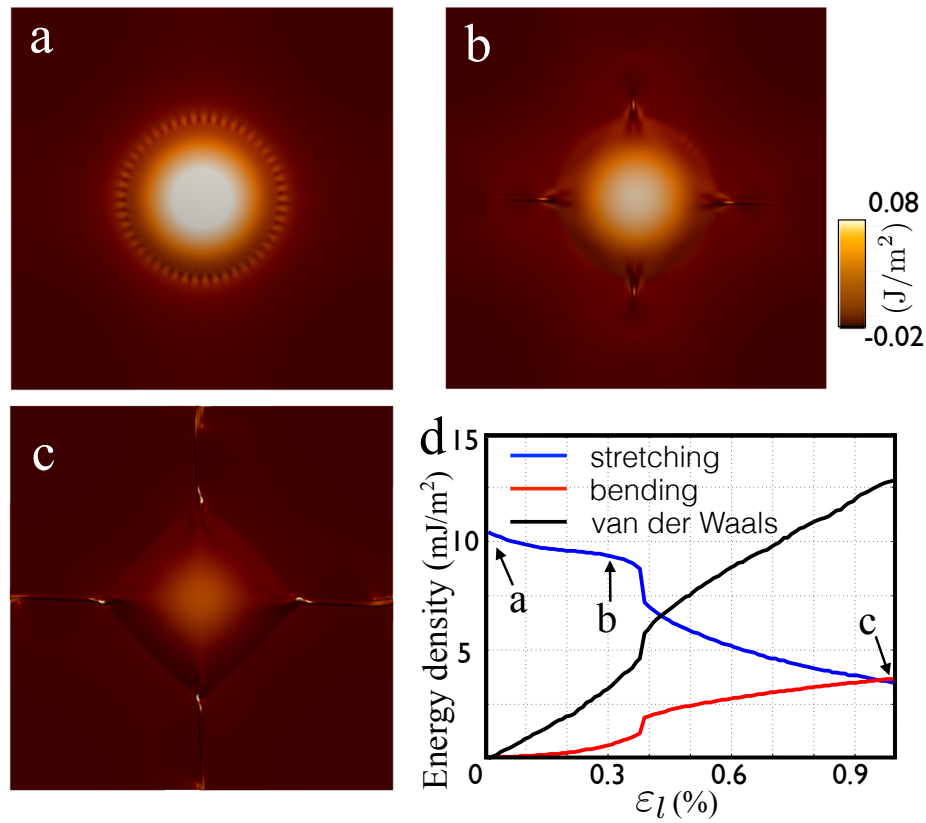

Figure 6.4: (a-c) In-plane stretching energy density during the transition from a circular bubble into a straight-edged bubble, shown earlier in Fig. 6.2 (i-iii). (d) A plot of different energy components when the applied compressive strain is increased.

induced from a defect on the substrate without having to exit the meta-stability region of the planar state.

We discussed in Chapt. 4 that wrinkle network formation could be interpreted as a process of stretching energy relaxation and focusing. To analyze whether analogous mechanisms are also operative here, we investigate next the energetics of the transition between a circular bubble and a straight-edged bubble associated to wrinkles, as shown in Fig. 6.2(i-iii). A quasi-spherical bubble is doubly curved, and therefore Gauss Egregium Theorem implies that such configurations are necessarily stretched, see Sec. 3. Such stretching is energetically penalized by graphene's extreme in-plane stiffness. Figure 6.4(a) shows the stretching energy density, which is significant (compare with Fig. 4.2 in Chapt. 4) and spreads over the entire bubble and part of the adhered region in its vicinity. This figure also shows how the system partially relaxes the stretching energy at the periphery of the bubble by slightly rip-

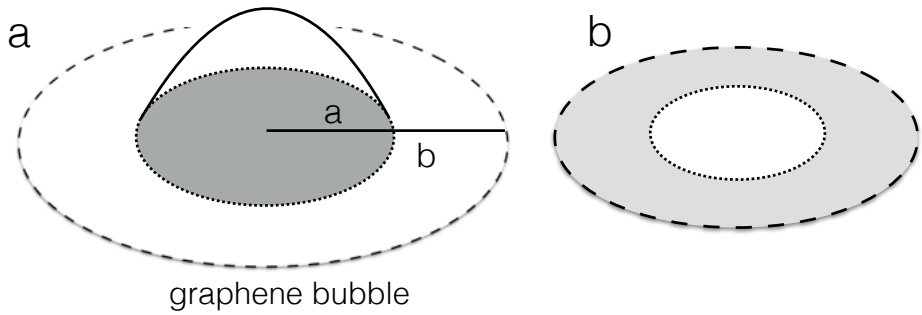

Figure 6.5: We divide an adhered circular region with a bubble into two parts: (a) the bubble and (b) the external annular region.

pling. Figure 6.4(b) shows how, as strain is progressively increased, the transition towards a straight-edged bubble with radial wrinkles relaxes the stretching energy in the blister, but focuses stretching energy in small regions where the bubbles and wrinkles meet. When the bubble us fully polygonal, Fig. 6.4(c), this mechanism is exacerbated with nearly zero stretching energy throughout the sample, except for a weakly stretched region at the top of the bubble and tiny but highly stretched features at the wrinkle-bubble connections. Figure 6.4(d) shows the variations of the different components of the energy (in-plane stretching, bending and adhesion) per unit area as a function of compressive strain. The sharp drop in stretching energy in this plot corresponds to the moment when the wrinkles extend to the boundary of the periodic domain. These results confirm the depiction of this process as one of stretching energy relaxation and focusing, at the expense of bending and adhesion energy.

A critical step in the transition from circular to straight-edged bubbles is the nucleation of short wrinkles at the periphery of the bubble. We analyze next in detail the stress state in this region for a circular bubble to shed light into the onset of this process.

3 A membrane analysis

During this transition from circular to straight-edged bubbles, thin and short wrinkles nucleate near the periphery of the bubble. This buckling event is governed by the biaxial strain conditions near the periphery of the bubble. To examine this process, we develop next an analytical model, related to previous membrane analyses of supported graphene bubbles (Yue et al., 2012; Koenig et al., 2011).

Previous membrane analyses of supported graphene bubbles usually assume a clamped boundary condition of the bubble edge, and thus zero hoop strain where wrinkles form. However, a compressive hoop strain can develop due to the the sliding of the bubble boundary (Kitt et al., 2013). The compressive hoop strain near the periphery of the bubble can trigger the nucleation of wrinkles. Here, we consider this in-plane sliding of graphene near the bubble edge, and include in the analysis the outer annular region of graphene adhered to the substrate, see Fig. 6.5(a). As commonly done (Yue et al., 2012), we assume the out-of-plane profile of the bubble as

$$z(r) = \delta\left(1 - \frac{r^2}{a^2}\right), \tag{6.5}$$

for an axisymmetric bubble of radius a and maximum deflection δ, both to be determined. We assume a cubic distribution of radial displacement

$$u(r) = \left(u_0 + u_1\frac{r}{a}\right)\frac{r}{a}\left(1 - \frac{r}{a}\right) + u_p\frac{r}{a}, \tag{6.6}$$

where u_0 and u_1 are the parameters to be determined, and u_p accounts for the in-plane sliding of the circle. Equations (6.5) and (6.6) offer a reasonable approximation for the deformation of relatively large bubbles. In the von Karman theory, accounting for the nonlinear effect of the out-of-plane displacement $z(r)$, the radial and hoop strains adopt the form (Landau and Lifshitz, 1959)

$$\varepsilon_r(r) = \frac{\partial u}{\partial r}(r) + \frac{1}{2}\left[\frac{\partial z}{\partial r}(r)\right]^2, \tag{6.7}$$

$$\varepsilon_t(r) = \frac{u(r)}{r}. \tag{6.8}$$

Recalling Equations (6.5) and (6.6), the radial and hoop strain can be written as

$$\varepsilon_r(r) = \left(\frac{u_0}{a} + \frac{u_1 r}{a^2}\right)\left(1 - \frac{2r}{a}\right) + \frac{u_1 r}{a^2}\left(1 - \frac{r}{a}\right) + \frac{2\delta^2 r^2}{a^4} + \frac{u_p}{a}, \tag{6.9}$$

$$\varepsilon_t(r) = \left(\frac{u_0}{a} + \frac{u_1 r}{a^2}\right)\left(1 - \frac{r}{a}\right) + \frac{u_p}{a}. \tag{6.10}$$

Note that the hoop strain in Equation (6.10) is in general not zero at the periphery ($r = a$), as controlled by the sliding displacement u_p. We can now derive the elastic strain energy per unit area as

$$U_s^{in}(r) = \frac{E_{2D}}{2(1-\nu^2)}(\varepsilon_r^2 + 2\nu\varepsilon_r\varepsilon_t + \varepsilon_t^2). \tag{6.11}$$

In the current membrane model, we ignore the bending stiffness of the film. This approximation is computationally convenient and is valid for relatively large bubbles. The pressure of gas inside the bubble has the following contribution of free energy density,

$$U_g(r) = -z\Delta p. \tag{6.12}$$

Next, we consider the annular region outside of the bubble, which is adhered to the substrate, and has the inner radius a, and outer radius b, see Fig. 6.5(b). The radial and hoop components of stress follow the general form (Landau and Lifshitz, 1959)

$$\begin{aligned} \sigma_r &= \frac{A}{r^2} + 2C, \\ \sigma_t &= -\frac{A}{r^2} + 2C, \end{aligned} \tag{6.13}$$

and the radial displacement in the region $a < r < b$ is

$$u = \frac{1}{E_{2D}}\left[-\frac{(1+\nu)A}{r} + 2C(1-\nu)r\right]. \tag{6.14}$$

In this region, we impose the Dirichlet boundary conditions $u_{r=b} = \varepsilon_l b$ and $u_{r=a} = u_p$, see Equation (6.6). Combining these boundary conditions with Equation (6.14), we obtain

$$A = \frac{E_{2D}}{1+\nu}\frac{ab^2}{b^2-a^2}(u_p - a\varepsilon_l), \tag{6.15}$$

$$2C = \frac{E_{2D}}{1-\nu}\frac{b^2\varepsilon_l - au_p}{b^2-a^2}. \tag{6.16}$$

Recalling Equation (6.13) and the expressions for A and C, we can compute stretching energy density of the annular region outside of the bubble as

$$U_s^{out}(r) = \frac{1}{2E_{2D}}(\sigma_r^2 + \sigma_t^2) - \frac{\nu}{E_{2D}}\sigma_r\sigma_t. \tag{6.17}$$

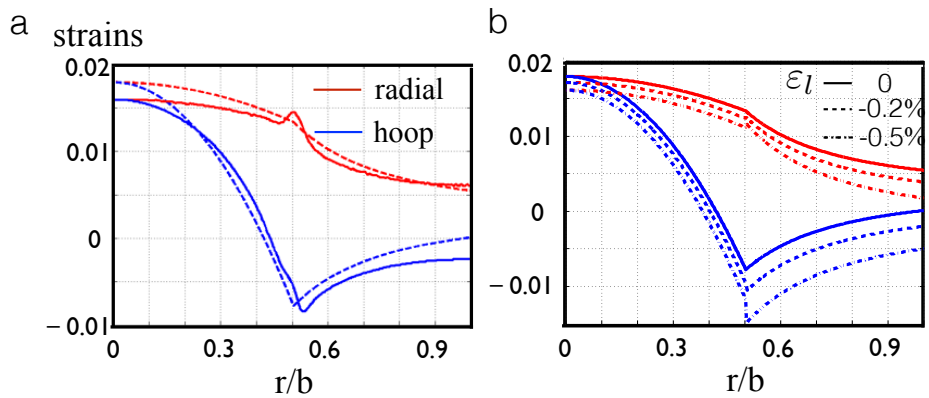

Figure 6.6: (a) Comparison between the theoretical model (dotted lines) and the nonlinear simulations (solid lines) for the radial and hoop components of the strain. (b) Distribution of the radial and hoop components of the strain when the applied strain ε_l is progressively increased. The hoop strain develops increasing compression near the periphery of the bubble.

Considering now the entire system consisting of the bubble and the annular region, and including the effect of the adhesion energy per unit surface γ, we obtain the total energy as

$$\Pi(a, \delta, u_0, u_1, u_p) = 2\pi \int_0^a \left(U_s^{in} + U_g\right) r dr + 2\pi \int_a^b \left(U_s^{out} + \gamma\right) r dr. \tag{6.18}$$

By minimizing the total energy Equation (6.18) with respect of a, δ, u_0, u_1, u_p, stable equilibria are obtained. The distribution of two components of strain is shown in Fig. 6.6(a), and compared with our nonlinear simulations. Despite the simplicity of the theoretical model, the fact that our periodic computational domain is square (as opposed to the disc-like geometry of the simple model), and the modest size of the bubble (and therefore bending energy plays a role), the agreement between model and simulations is quite good. We see that at the periphery of the bubble, the strain is negative (compressive) in hoop direction, and positive in radial direction. These negative hoop strains are consistent with the small ripples always present in our simulations in at the edge of the detached part of quasi-spherical bubbles. The model also shows that the compressive hoop strain increases as ε_l increases. Such high compressive hoop strains could favor the nucleation of small wrinkles near the periphery of the bubble, and trigger the morphological evolution from a circular bubble to a straight-edged bubble in Fig. 6.2(i-iii). We analyze next the onset of instability for an adhered elastic sheet with compressive strain in one direction and tensile strain in the perpendicular direction, representative of the state at the periphery of the bubble, to

estimate the onset of this instability.

4 Buckling analysis at the periphery of the bubble

For supported graphene under uniaxial compression, a linear instability analysis has been proposed in many previous studies, predicting a critical strain upon which the planar surface transforms to rippling. With further compression, the uniformly distributed rippling will transit to several localized wrinkles due to the nonlinearity of van der Waals interaction (Zhang and Arroyo, 2013). As we discussed previously, the periphery region of bubble experiences a biaxial strain state, compressive along the azimuthal direction and tensile in the radial direction. We examine next the onset of buckling under such biaxial strain, ignoring details such as the curvature of the bubble edge.

Consider a supported rectangular graphene sheet compressed in one direction and stretched in the other direction Fig. 6.7(a). The stretching delays the critical strain of rippling without changing the rippling direction or wavelength. We denote by $u(x, y)$ and $v(x, y)$ the in-plane displacements and $w(x, y)$ the out-of-plane displacement of the membrane, and ε_x and ε_y the in-plane strain components in x and y directions. The stretching and bending energies of the membrane per unit area can be expressed as

$$\begin{aligned} U_s =& \frac{\bar{Y}}{2}(\varepsilon_x^2 + \varepsilon_y^2 + 2\nu\varepsilon_x\varepsilon_y), \\ U_b =& \frac{D}{2}\left(\frac{\partial^2 w}{\partial x^2}\right)^2. \end{aligned} \tag{6.19}$$

Adopting a von Karman nonlinear plate theory (Landau and Lifshitz, 1959), the membrane strain components of the film can be approximated as

$$\begin{aligned} \varepsilon_x &= \varepsilon_x^0 + \frac{\partial u}{\partial x} + \frac{1}{2}\left(\frac{\partial w}{\partial x}\right)^2, \\ \varepsilon_y &= \varepsilon_y^0 + \frac{\partial v}{\partial y} + \frac{1}{2}\left(\frac{\partial w}{\partial y}\right)^2, \end{aligned} \tag{6.20}$$

where ε_x^0 and ε_y^0 represent the globally applied lateral strain on the membrane. We assume uniaxial ripples perpendicular to the direction of compressive strain as $w(x) = A\cos(kx)$. By requiring the uniformity of the in-plane tension or strain, see Eq. (6.20), the in-plane

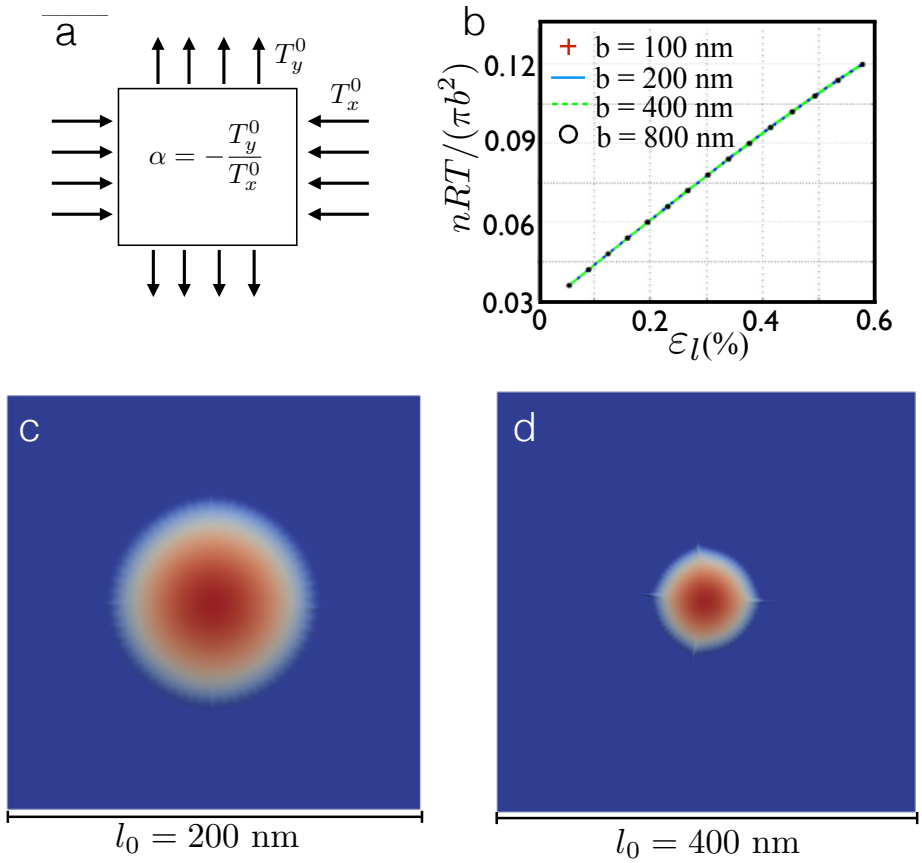

Figure 6.7: (a) Simplified model for the state of the graphene sheet at the periphery of the bubble, under compression in the x direction (the azimuthal direction) and stretching in y (radial) direction. (b) An estimation of the boundary between the white (circular bubble) and light grey (straight-edged bubble with wrinkles) regions in the phase diagram in Fig. 6.2 with various sizes of the domain. As predicted by (b), under the same value of $nRT = 2500$ nN·nm and $\varepsilon_l = 0.15\%$, for an array of bubbles of high density (small domain size, c), the quasi-spherical bubble is more stable than for a lower density of bubbles (d).

displacement in x becomes $u(x) = (1/8)k^2A^2\sin(2kx)$, and the constant strain component in x becomes $\varepsilon_x = \varepsilon_x^0 + (1/4)k^2A^2$. In the y direction, $\varepsilon_y = \varepsilon_y^0$. The stretching energy difference per unit area takes the form

$$\begin{aligned}\Delta\bar{U}_s(A,k) =& \frac{\bar{Y}}{2}(\varepsilon_x^2 + \varepsilon_y^2 + 2\nu\varepsilon_x\varepsilon_y - {\varepsilon_x^0}^2 - {\varepsilon_y^0}^2 - 2\nu\varepsilon_x^0\varepsilon_y^0) \\ =& \frac{T_x^0}{4}k^2A^2 + \frac{\bar{Y}}{32}k^4A^4 + \frac{T_y^0}{4}\nu k^2A^2,\end{aligned} \tag{6.21}$$

where $T_x^0 = \bar{Y}\varepsilon_x^0$ and $T_y^0 = \bar{Y}\varepsilon_y^0$ are reference surface tensions in the x and y directions. The third term in Eq. (6.21) is the contribution in the stretching energy of the applied stretch in the y direction. Including the bending and adhesion energies, the total energy difference per unit area then becomes

$$\Delta\bar{U}(A,k) = \left(\frac{T_x^0 + T_y^0\nu}{4}k^2 + \frac{D}{4}k^4 + \frac{27\gamma}{4h_0^2}\right)A^2 + \frac{\bar{Y}}{32}k^4A^4. \tag{6.22}$$

If $T_y^0 = -\alpha T_x^0$, we have

$$\varepsilon_{cr} = -\frac{2}{h_0\bar{Y}(1-\alpha\nu)}\sqrt{27\gamma D}, \tag{6.23}$$

which predicts the critical strain along x.

The theory developed in Sec. 3 provides an estimate of the strain state at the periphery of the bubble, i.e. ε_x and α, given the applied strain ε_l and nRT. Using the equation above to estimate the onset of buckling instability at the margin of a quasi-spherical bubble, we can theoretically estimate the boundary between the white (circular bubble) and light grey (straight-edged bubble with wrinkles) regions in the phase diagram in Fig. 6.2. This theoretical estimate of the boundary is represented in Fig. 6.7(b). Despite all the approximations in the model and the somewhat arbitrary criterion to select the boundary in Fig. 6.2, we observe that the numerical and theoretical boundaries agree quite well. Interestingly, it can be observed that when plotting nRT per unit area versus ε_l, the boundary does not change as the size of the domain changes. Since the size of the domain can be interpreted as the separation between bubbles in a graphene sample, we can conclude that the transition strain between circular and straight-edged bubbles for a given number of trapped molecules per unit graphene area is independent of bubble density. This observation allows us to estimate the transition from circular bubbles to straight-edged bubbles for very large domain sizes,

beyond the limits of our computational capabilities. The relation represented in Fig. 6.7(b) predicts that for a given nRT and ε_l, circular bubbles are more stable if the domain size is smaller. Figures 6.7(c) and 6.7(d) show an example of this behavior, where for the larger domain size, wrinkles have nucleated at the periphery of the bubble.

Contributions

We summarize here the most significant contributions of this chapter:

1. We have examined the coexistence of wrinkles and blisters in supported graphene. We have shown that a wide diversity of out-of-plane disturbances observed in supported graphene, including spherical bubbles, wrinkles, and polygonal blisters, can be explained within a unified framework accounting for the lateral strain and for the trapped mass beneath the graphene sample.

2. We have proposed a morphological diagram organizing the behavior of the system.

3. The transition between quasi-spherical bubbles to straight-edged bubbles upon increasing compressive strain can be understood as a process of stretching energy relaxation and focusing. A simple theoretical model suggest that the onset of this transition is determined by compressive hoop strains at the periphery of the bubble caused by radial sliding. This model predicts that the critical compressive strain to transition between circular and straight-edged bubbles for a given number of trapped molecules per unit graphene area is independent of bubble density.

Chapter 7

Conclusions

We have examined various aspects of the mechanics of out-of-plane deformations in supported graphene upon uniaxial or biaxial strains, and under the pressure produced by trapped gas molecules. The main contributions of the present work are summarized below:

1. We have studied the emergence of spontaneous wrinkling in supported and uniaxially strained graphene with high-fidelity simulations based on an atomistically-informed continuum model.

2. With a simpler theoretical model, we have characterized the onset of buckling and the nonlinear behavior after the instability in terms of the adhesion and frictional material parameters of the graphene-substrate interface. We have found that localized wrinkles evolve from a distributed rippling linear instability due to the nonlinearity in the van der Waals graphene-substrate interactions.

3. When graphene sample is supported on a tight substrate, e.g. silicon-oxide, and upon compression, localized wrinkles develop from the planar state without an observable rippling stage, in agreement with experiments.

4. We identify friction as a selection mechanism for the separation between wrinkles, as the formation of far apart wrinkles is penalized by the work of friction. We quantitively study the separation distance between wrinkles in terms of the interfacial shear strength in the interface (friction) theoretically and by simulations.

5. We have reproduced computationally the most salient features of wrinkle networks observed in supported graphene upon biaxial strains. We have identified the influence of strain anisotropy and the adhesive and frictional properties on the morphology of spontaneously-formed wrinkle networks.

6. We have proposed a method to precisely control the location of wrinkles through patterns of stripes of weaker adhesion on the substrate.

7. We have assessed the connectivity and stability of the networks of channels trapping fluid molecules, opening the door to nano-fluidic applications.

8. We have examined the coexistence of wrinkles and blisters in supported graphene. Considering both applied strains and trapped mass beneath the graphene sample, we have built a morphological diagram determining the relative stability of quasi-spherical bubbles, of straight-edged bubbles coexisting with wrinkles, and of wrinkle networks.

This work also suggests open research topics for the future:

1. We have focused here on supported graphene sheets under compression. Under tension or subject to out-of-plane forces, however, graphene can fracture and peel (Sen et al., 2010). This fracture behavior can be important to assess the reliability of devices or as a fabrication method. It could be modeled by introducing a fracture phase-field model, possibly with an anisotropic fracture energy (Li et al., 2014).

2. The strong coupling between localized deformation and electronic structure of supported graphene is another interesting topic. The electronic and quantum effects due to localized strains resulting from buckling, e.g. at junctions of wrinkle networks, need to be evaluated.

3. Besides of the elastic buckling in wrinkles and blisters, other types of structural defects such as dislocations, grain boundaries, or bridges between multilayer graphene could be considered in the simulations, to depict a broader picture of out-of-plane deformations of supported graphene.

4. More general aspects of the substrate could be studied. In the thesis, graphene samples are supported on a stiff substrate, which is assumed planar in the simulations. By

considering a soft substrate, the coherent buckling of graphene and substrate surface near the interface can be evaluated. Besides, the deformability of the substrate in the tangential direction could be accounted for with a shear-lag model coupled with friction and extended to biaxial situations.

Bibliography

Aitken, Z. H. and R. Huang (2010). Effects of mismatch strain and substrate surface corrugation on morphology of supported monolayer graphene. *Journal of Applied Physics 107*(12), 123531.

Aoyanagi, Y., J. Hure, J. Bico, and B. Roman (2010). Random blisters on stickers: metrology through defects. *Soft Matter 6*, 5720–5728.

Arias, I. and M. Arroyo (2008). Size-dependent nonlinear elastic scaling of multiwalled carbon nanotubes. *Phys. Rev. Lett. 100*, 085503.

Arroyo, M. and T. Belytschko (2002). An atomistic-based finite deformation membrane for single layer crystalline films. *Journal of the Mechanics and Physics of Solids 50*(9), 1941–1977.

Arroyo, M. and T. Belytschko (2003). Nonlinear mechanical response and rippling of thick multi-walled carbon nanotubes. *Physical Review Letters 91*(21), 215505.

Arroyo, M. and T. Belytschko (2004a). Finite crystal elasticity of carbon nanotubes based on the exponential cauchy-born rule. *Physical Review B 69*, 115415.

Arroyo, M. and T. Belytschko (2004b). Finite element methods for the non-linear mechanics of crystalline sheets and nanotubes. *Int. J. Numer. Meth. Engng 59*(3), 419–456.

Audoly, B. (2011, Jul). Localized buckling of a floating elastica. *Phys. Rev. E 84*, 011605.

Bao, W., F. Miao, Z. Chen, H. Zhang, W. Jang, C. Dames, and C. N. Lau (2009). Controlled ripple texturing of suspended graphene and ultrathin graphite membranes. *Nat Nano 4*, 562–566.

Boddeti, N. G., X. Liu, R. Long, J. Xiao, J. S. Bunch, and M. L. Dunn (2013). Graphene blisters with switchable shapes controlled by pressure and adhesion. *Nano Letters 13*(12), 6216–6221.

Bourlon, B., D. C. Glattli, C. Miko, L. Forró, and A. Bachtold (2004). Carbon nanotube based bearing for rotational motions. *Nano Letters 4*(4), 709–712.

Brau, F., H. Vandeparre, A. Sabbah, C. Poulard, A. Boudaoud, and P. Damman (2011). Multiple-length-scale elastic instability mimics parametric resonance of nonlinear oscillators. *Nat Phys 7*, 56–60.

Brenner, D. (1990). Empirical potential for hydrocarbons for use in simulating chemical vapor deposition of diamond films. *Physical Review B 42*(15), 9458–9471.

Bunch, J. S., A. M. van der Zande, S. S. Verbridge, I. W. Frank, D. M. Tanenbaum, J. M. Parpia, H. G. Craighead, and P. L. McEuen (2007). Electromechanical resonators from graphene sheets. *Science 315*(5811), 490–493.

Bunch, J. S., S. S. Verbridge, J. S. Alden, A. M. van der Zande, J. M. Parpia, H. G. Craighead, and P. L. McEuen (2008). Impermeable atomic membranes from graphene sheets. *Nano Letters 8*(8), 2458–2462.

Calado, V. E., G. F. Schneider, A. M. M. G. Theulings, C. Dekker, and L. M. K. Vandersypen (2012). Formation and control of wrinkles in graphene by the wedging transfer method. *Applied Physics Letters 101*(10), 103116.

Cao, Y., B. Li, and X. Feng (2012). Surface wrinkling and folding of core-shell soft cylinders. *Soft Matter 8*, 556–562.

Castellanos-Gomez, A., R. Roldán, E. Cappelluti, M. Buscema, F. Guinea, H. S. J. van der Zant, and G. A. Steele (2013). Local strain engineering in atomically thin mos2. *Nano Letters doi: 10.1021/nl402875m*.

Cerda, E., S. Chaieb, F. Melo, and L. Mahadevan (1999). Conical dislocations in crumpling. *Nature 401*, 46–49.

Chen, X. and J. W. Hutchinson (2004). Herringbone buckling patterns of compressed thin films on compliant substrates. *Journal of Applied Mechanics 71*, 597–603.

Cirak, F., M. Ortiz, and P. Schröder (2000). Subdivision surfaces: a new paradigm for thin-shell finite-element analysis. *International Journal for Numerical Methods in Engineering 47*, 2039–2072.

Cumings, J. and A. Zettl (2000). Low-friction nanoscale linear bearing realized from multi-wall carbon nanotubes. *Science 289*(5479), 602–604.

Duan, W., K. Gong, and Q. Wang (2011). Controlling the formation of wrinkles in a single layer graphene sheet subjected to in-plane shear. *Carbon 49*, 3107–3112.

Duong, D. L., G. H. Han, S. M. Lee, F. Gunes, E. S. Kim, S. T. Kim, H. Kim, Q. H. Ta, K. P. So, S. J. Yoon, S. J. Chae, Y. W. Jo, M. H. Park, S. H. Chae, S. C. Lim, J. Y. Choi, and Y. H. Lee (2012). Probing graphene grain boundaries with optical microscopy. *Nature 490*, 235–239.

Gao, W. and R. Huang (2011). Effect of surface roughness on adhesion of graphene membranes. *Journal of Physics D: Applied Physics 44*, 452001.

Garcia-Pomar, J. L., A. Y. Nikitin, and L. Martin-Moreno (2013). Scattering of graphene plasmons by defects in the graphene sheet. *ACS Nano 7*(6), 4988–4994.

Georgiou, T., L. Britnell, P. Blake, R. V. Gorbachev, A. Gholinia, A. K. Geim, C. Casiraghi, and K. S. Novoselov (2011). Graphene bubbles with controllable curvature. *Applied Physics Letters 99*(9), 093103.

Ghosh, S. and M. Arroyo (2013). An atomistic-based foliation model for multilayer graphene materials and nanotubes. *Journal of the Mechanics and Physics of Solids 61*, 235–253.

Girifalco, L. A., M. Hodak, and R. S. Lee (2000). Carbon nanotubes, buckyballs, ropes, and a universal graphitic potential. *Physical Review B 62*(19), 13104–13110.

Gong, L., I. A. Kinloch, R. J. Young, I. Riaz, R. Jalil, and K. S. Novoselov (2010). Interfacial stress transfer in a graphene monolayer nanocomposite. *Adv. Mater. 22*, 2694–2697.

Guinea, F., M. I. Katsnelson, and A. K. Geim (2010). Energy gaps and a zero-field quantum hall effect in graphene by strain engineering. *Nat Phys 6*, 30–33.

Guo, X., J. Wang, and H. Zhang (2006). Mechanical properties of single-walled carbon nanotubes based on higher order cauchyâborn rule. *International Journal of Solids and Structures 43*(5), 1276 – 1290.

Gupta, A., G. Chen, P. Joshi, S. Tadigadapa, and Eklund (2006). Raman scattering from high-frequency phonons in supported n-graphene layer films. *Nano Letters 6*(12), 2667–2673.

Hendricks, T. R., W. Wang, and I. Lee (2010). Buckling in nanomechanical films. *Soft Matter 6*, 3701–3706.

Holmes, D. and A. Crosby (2003). Draping films: A wrinkle to fold transition. *Physical Review Letters 105*, 038303.

Huang, X. and S. Zhang (2011). Morphologies of monolayer graphene under indentation. *Modelling and Simulation in Materials Science and Engineering 19*(5), 054004.

Huang, Z. Y., W. Hong, and Z. Suo (2005). Nonlinear analyses of wrinkles in a film bonded to a compliant substrate. *Journal of the Mechanics and Physics of Solids 53*, 2101–2118.

Im, S. H. and R. Huang (2008). Wrinkle patterns of anisotropic crystal films on viscoelastic substrates. *Journal of the Mechanics and Physics of Solids 56*(12), 3315–3330.

Jiang, T., R. Huang, and Y. Zhu (2013). Interfacial sliding and buckling of monolayer graphene on a stretchable substrate. *Advanced Functional Materials 24*, 396–402.

Kim, E.-A. and A. H. C. Neto (2008). Graphene as an electronic membrane. *EPL (Europhysics Letters) 84*(5), 57007.

Kim, K., Z. Lee, B. D. Malone, K. T. Chan, B. Alemán, W. Regan, W. Gannett, M. F. Crommie, M. L. Cohen, and A. Zettl (2011). Multiply folded graphene. *Phys. Rev. B 83*, 245433.

Kim, P., M. Abkarian, and H. A. Stone (2011). Hierarchical folding of elastic membranes under biaxial compressive stress. *Nat Mater 10*, 952–957.

Kitt, A. L., Z. Qi, S. Rémi, H. S. Park, A. K. Swan, and B. B. Goldberg (2013). How graphene slides: Measurement and theory of strain-dependent frictional forces between graphene and sio2. *Nano Letters 13*(6), 2605–2610.

Koenig, S. P., N. G. Boddeti, M. L. Dunn, and J. S. Bunch (2011). Ultrastrong adhesion of graphene membranes. *Nat Nano 6*, 543–546.

Landau, L. D. and E. M. Lifshitz (1959). *Theory of Elasticity*. Pergamon.

Landau, L. D. and E. M. Lifshitz (1980). *Statistical Physics Part I*. Pergamon.

Leahy, B. D., L. Pocivavsek, M. Meron, K. L. Lam, D. Salas, P. J. Viccaro, K. Y. C. Lee, and B. Lin (2010). Geometric stability and elastic response of a supported nanoparticle film. *Phys. Rev. Lett. 105*, 058301.

Lee, C., Q. Li, W. Kalb, X. Liu, H. Berger, R. W. Carpick, and J. Hone (2010). Frictional characteristics of atomically thin sheets. *Science 328*(5974), 76–80.

Lee, C., X. Wei, J. W. Kysar, and J. Hone (2008). Measurement of the elastic properties and intrinsic strength of monolayer graphene. *Science 321*, 385–388.

Lee, C., X. Wei, Q. Li, R. Carpick, J. W. Kysar, and J. Hone (2009). Elastic and frictional properties of graphene. *Phys. Status Solidi B 246*(11-12), 2562–2567.

Levy, N., S. A. Burke, K. L. Meaker, M. Panlasigui, A. Zettl, F. Guinea, A. H. C. Neto, and M. F. Crommie (2010). Strain-induced pseudo–magnetic fields greater than 300 tesla in graphene nanobubbles. *Science 329*(5991), 544–547.

Li, B., C. Peco, D. Millán, I. Arias, and M. Arroyo (2014). Phase-field modeling and simulation of fracture in brittle materials with strongly anisotropic surface energy. *International Journal for Numerical Methods in Engineering*, n/a–n/a.

Li, X., W. Cai, J. An, S. Kim, J. Nah, D. Yang, R. Piner, A. Velamakanni, I. Jung, E. Tutuc, S. K. Banerjee, L. Colombo, and R. S. Ruoff (2009). Large-area synthesis of high-quality and uniform graphene films on copper foils. *Science 324*(5932), 1312–1314.

Liu, M., Y. Zhang, Y. Chen, Y. Gao, T. Gao, D. Ma, Q. Ji, Y. Zhang, C. Li, and Z. Liu (2012). Thinning segregated graphene layers on high carbon solubility substrates of rhodium foils by tuning the quenching process. *ACS Nano 6*(12), 10581–10589.

Liu, N., Z. Pan, L. Fu, C. Zhang, B. Dai, and Z. Liu (2011). The origin of wrinkles on transferred graphene. *Nano Research 4*, 996–1004.

Liu, X., N. G. Boddeti, M. R. Szpunar, L. Wang, M. A. Rodriguez, R. Long, J. Xiao, M. L. Dunn, and J. S. Bunch (2013). Observation of pull-in instability in graphene membranes under interfacial forces. *Nano Letters 13*(5), 2309–2313.

Liu, Y. and B. I. Yakobson (2010). Cones, pringles, and grain boundary landscapes in graphene topology. *Nano Letters 10*(6), 2178–2183.

Lu, Q., M. Arroyo, and R. Huang (2009). Elastic bending modulus of monolayer graphene. *Journal of Physics D: Applied Physics 42*, 102002.

Meyer, J. C., A. K. Geim, M. I. Katsnelson, K. S. Novoselov, T. J. Booth, and S. Roth (2007). The structure of suspended graphene sheets. *Nature 446*, 60–63.

Nelson, D. and L. Peliti (1987). Fluctuations in membranes with crystalline and hexatic order. *J. Phys. 48*, 1085–1092.

Novoselov, K. S., A. K. Geim, S. V. Morozov, D. Jiang, Y. Zhang, S. V. Dubonos, I. V. Grigorieva, and A. A. Firsov (2004). Electric field effect in atomically thin carbon films. *Science 306*(5696), 666–669.

Obraztsov, A. N., E. A. Obraztsova, A. V. Tyurnina, and A. A. Zolotukhin (2007). Chemical vapor deposition of thin graphite films of nanometer thickness. *Carbon 45*, 2017–2021.

Pan, W., J. Xiao, J. Zhu, C. Yu, G. Zhang, Z. Ni, K. Watanabe, T. Taniguchi, Y. Shi, and X. Wang (2012). Biaxial compressive strain engineering in graphene/boron nitride heterostructures. *Sci. Rep. 2*, 893.

Pan, Z., N. Liu, L. Fu, and Z. Liu (2011). Wrinkle engineering: A new approach to massive graphene nanoribbon arrays. *Journal of the American Chemical Society 133*(44), 17578–17581.

Peierls, R. E. (1935). Quelques proprietes typiques des corpses solides. *Ann. Inst. Henri Poincare 5*, 177–222.

Pereira, V. M., A. H. Castro Neto, H. Y. Liang, and L. Mahadevan (2010, Oct). Geometry, mechanics, and electronics of singular structures and wrinkles in graphene. *Phys. Rev. Lett. 105*, 156603.

Pocivavsek, L., R. Dellsy, A. Kern, S. Johnson, B. Lin, K. Y. C. Lee, and E. Cerda (2008). Stress and fold localization in thin elastic membranes. *Science 320*, 912–916.

Prakash, G., M. A. Capano, M. L. Bolen, D. Zemlyanov, and R. G. Reifenberger (2010). {AFM} study of ridges in few-layer epitaxial graphene grown on the carbon-face of 4häìsic. *Carbon 48*(9), 2383 – 2393.

Pugno, N., Q. Yin, X. Shi, and R. Capozza (2013). A generalization of the coulomb friction law: from graphene to macroscale. *Meccanica 48*(8), 1845–1851.

Rahimi, M., K. Zhang, and M. Arroyo (2015). Computing the volume enclosed by a periodic surface and its variation to model a follower pressure. *Computational Mechanics*, 1–7.

Robertson, A. W., A. Bachmatiuk, Y. A. Wu, F. Schäffel, B. Büchner, M. H. Rümmeli, and J. H. Warner (2011). Structural distortions in few-layer graphene creases. *ACS Nano 5*(12), 9984–9991.

Ruoff, R. (2012). Perspective: A means to an end. *Nature 483*(7389), S42.

Scharfenberg, S., N. Mansukhani, C. Chialvo, R. L. Weaver, and N. Mason (2012). Observation of a snap-through instability in graphene. *Applied Physics Letters 100*(2), 021910.

Sen, D., K. S. Novoselov, P. M. Reis, and M. J. Buehler (2010). Tearing Graphene Sheets From Adhesive Substrates Produces Tapered Nanoribbons. *Small 6*, 1108–1116.

Shenoy, V., R. Miller, E. Tadmor, R. Phillips, and M. Ortiz (1998). Quasicontinuum models of interfacial structure and deformation. *Physical Review Letters 80*, 742–745.

Smith, G., E. Tadmor, and E. Kaxiras (2000). Multiscale simulation of loading and electrical resistance in silicon nanoindentation. *Physical Review Letters 84*(6), 1260–1263.

Stolyarova, E., D. Stolyarov, K. Bolotin, S. Ryu, L. Liu, K. T. Rim, M. Klima, M. Hybertsen, I. Pogorelsky, I. Pavlishin, K. Kusche, J. Hone, P. Kim, H. L. Stormer, V. Yakimenko, and G. Flynn (2009). Observation of graphene bubbles and effective mass transport under graphene films. *Nano Letters 9*(1), 332–337.

Tadmor, E., G. Smith, N. Bernstein, and E. Kaxiras (1999). Mixed finite element and atomistic formulation for complex crystals. *Physical Review B 59*(1), 235–245.

Vandeparre, H., J. Léopoldès, C. Poulard, S. Desprez, G. Derue, C. Gay, and P. Damman (2007, Oct). Slippery or sticky boundary conditions: Control of wrinkling in metal-capped thin polymer films by selective adhesion to substrates. *Phys. Rev. Lett. 99*, 188302.

Wang, P., W. Zhang, O. Liang, M. Pantoja, J. Katzer, T. Schroeder, and Y.-H. Xie (2012). Giant optical response from graphene–plasmonic system. *ACS Nano 6*(7), 6244–6249. PMID: 22712497.

Wang, Y., R. Yang, Z. Shi, L. Zhang, D. Shi, E. Wang, and G. Zhang (2011). Super-elastic graphene ripples for flexible strain sensors. *ACS Nano 5*(5), 3645–3650.

Warner, J. H., Y. Fan, A. W. Robertson, K. He, E. Yoon, and G. D. Lee (2013). Rippling graphene at the nanoscale through dislocation addition. *Nano Letters 13*(10), 4937–4944.

Whitby, M. and N. Quirke (2007). Fluid flow in carbon nanotubes and nanopipes. *Nat Nano 2*, 87–94.

Witten, T. A. (2007, Apr). Stress focusing in elastic sheets. *Rev. Mod. Phys. 79*, 643–675.

Wu, J., K. C. Hwang, and Y. Huang (2008). An atomistic-based finite-deformation shell theory for single-wall carbon nanotubes. *Journal of the Mechanics and Physics of Solids 56*, 279–292.

Xu, K., P. Cao, and J. R. Heath (2009). Scanning tunneling microscopy characterization of the electrical properties of wrinkles in exfoliated graphene monolayers. *Nano Letters 9*, 4446–4451.

Yakobson, B., C. Brabec, and J. Bernholc (1996). Nanomechanics of carbon tubes: Instabilities beyond the linear response. *Physical Review Letters 76*(14), 2511–2514.

Yakobson, B. I. and F. Ding (2011). Observational geology of graphene, at the nanoscale. *ACS Nano 5*(3), 1569–1574.

Yoon, T., W. C. Shin, T. Y. Kim, J. H. Mun, T.-S. Kim, and B. J. Cho (2012). Direct measurement of adhesion energy of monolayer graphene as-grown on copper and its application to renewable transfer process. *Nano Letters 12*, 1448–1452.

Yu, M.-F., B. I. Yakobson, and R. S. Ruoff (2000). Controlled sliding and pullout of nested shells in individual multiwalled carbon nanotubes. *The Journal of Physical Chemistry B 104*(37), 8764–8767.

Yue, K., W. Gao, R. Huang, and K. M. Liechti (2012). Analytical methods for the mechanics of graphene bubbles. *Journal of Applied Physics 112*(8), –.

Zabel, J., R. R. Nair, A. Ott, T. Georgiou, A. K. Geim, K. S. Novoselov, and C. Casiraghi (2012). Raman spectroscopy of graphene and bilayer under biaxial strain: Bubbles and balloons. *Nano Letters 12*(2), 617–621.

Zang, J., S. Ryu, N. Pugno, Q. Wang, Q. Tu, M. J. Buehler, and X. Zhao (2013). Multifunctionality and control of the crumpling and unfolding of large-area graphene. *Nature Materials 12*, 321–325.

Zang, J., X. Zhao, Y. Cao, and J. W. Hutchinson (2012). Localized ridge wrinkling of stiff films on compliant substrates. *Journal of the Mechanics and Physics of Solids 60*, 1265–1279.

Zhang, K. and M. Arroyo (2013). Adhesion and friction control localized folding in supported graphene. *Journal of Applied Physics 113*(19), 193501.

Zhang, K. and M. Arroyo (2014). Understanding and strain-engineering wrinkle networks in supported graphene through simulations. *Journal of the Mechanics and Physics of Solids 72*(0), 61 – 74.

Zhang, S., S. L. Mielke, R. Khare, D. Troya, R. S. Ruoff, G. C. Schatz, and T. Belytschko (2005). Mechanics of defects in carbon nanotubes: Atomistic and multiscale simulations. *Phys. Rev. B 71*(11), 115403.

Zhang, T., X. Li, and H. Gao (2014). Defects controlled wrinkling and topological design in graphene. *Journal of the Mechanics and Physics of Solids 67*(0), 2 – 13.

Zhu, W., T. Low, V. Perebeinos, A. A. Bol, Y. Zhu, H. Yan, J. Tersoff, and P. Avouris (2012). Structure and electronic transport in graphene wrinkles. *Nano Letters 12*(7), 3431–3436.